Convection with Rotation in a Neutral Ocean: A Study of Open-Ocean Deep Convection

HELEN JONES AND JOHN MARSHALL

Center for Meteorology and Physical Oceanography, and Department of Earth, Atmospheric and Planetary Sciences, Massachusetts Institute of Technology, Cambridge, Massachusetts

(Manuscript received 26 December 1991, in final form 1 July 1992)

ABSTRACT

The intensity and scale of the geostrophically adjusted end state of the convective overturning of a homogeneous, rotating ocean of depth H at a latitude where the Coriolis parameter is f, induced by surface buoyancy loss of magnitude B_0, are studied by numerical experiment. The experiments are related to observations and laboratory studies of open-ocean deep convection. A numerical model based on the nonhydrostatic Boussinesq equations is used. The grid spacing of the model is small enough that gross aspects of convective plumes themselves can be resolved, yet the domain of integration is sufficiently large to permit study of the influence of plumes on the large scale and geostrophic adjustment of the convected water.

Numerical simulations suggest that cooling at the sea surface is offset by buoyancy drawn from depth through the agency of convective plumes. These plumes efficiently mix the water column to generate a dense chimney of fluid, which subsequently breaks up through the mechanism of baroclinic instability to form spinning cones of convectively modified water that have a well-defined and predictable scale.

A measure of the importance of rotation on the convective process is provided by a natural Rossby number introduced by Maxworthy and Narimousa:

$$\mathrm{Ro}^* = \frac{l_{\mathrm{rot}}}{H} = \frac{u_{\mathrm{rot}}}{fH} = \frac{B_0^{1/2}}{f^{3/2}H},$$

where $l_{\mathrm{rot}} = (B_0/f^3)^{1/2}$ is the length scale that marks the transition from three-dimensional, thermally driven turbulence to quasi-two-dimensional, rotationally dominated motions. Here $u_{\mathrm{rot}} = (B_0/f)^{1/2}$ is the velocity of a particle gyrating in inertial circles of radius l_{rot}.

In the parameter regime typical of open-ocean deep convection, we find that $\mathrm{Ro}^* \leqslant 1$; rotation influences the intensity and scale of both plumes and cones. In particular, the scale, intensity, buoyancy excess, and generation rate of the cones of geostrophically adjusted fluid, which result from the breakup of the chimney, are found to depend in a predictable way on this single nondimensional number, formed from the external parameters f, B_0, and H.

1. Introduction

Observations of open-ocean deep convection in the weakly stratified waters of the Gulf of Lions (Stommel et al. 1971; Schott and Leaman 1991) suggest that the convective process there is intermittent and takes place through a hierarchy of scales. The convective elements themselves we shall call *plumes.*[1] They carry fluid particles vertically over distances comparable to the depth of the ocean. Schott and Leaman (1991) estimate the horizontal scale of the plumes to be ~1 km. Driven by intense cooling at the sea surface reaching ~1000 W m^{-2}, they comprise both ascending and descending currents that reach speeds in excess of ~10 cm s^{-1}. Plumes penetrate most of the water column, efficiently homogenizing its properties. The deep, cold mixed layer (*chimney*) thus formed, maintained close to neutrality by the action of the plumes, sinks under gravity, geostrophically adjusts, and, on a time scale of a few days, is thought to break up into fragments. These fragments, which we shall call *cones,* are thought to have a spatial scale of some several kilometers.

The foregoing observations, reviewed in section 2, provide the motivation for the present study; by numerical experiment we investigate the convective overturning, in a population of plumes, of a homogeneous ocean of depth H induced by buoyancy loss of strength B_0 at its upper surface at a latitude where the Coriolis parameter is f. The end state of the convective process is an assembly of cold cones that extend through the whole depth of the ocean. We identify these

---

[1] We adopt the following nomenclature: *plumes* are the initial convective elements, the *chimney* is a collection of plumes, and *cones* are the residual pieces of the "broken" chimney.

Corresponding author address: Dr. John Marshall, Center for Meteorology and Physical Oceanography, Massachusetts Institute of Technology, Dept. of Earth, Atmospheric and Planetary Sciences, Building 54, Rm. 1526, Cambridge, MA 02139.

with the fragments of convectively tainted water seen in the observations. The cones have swirling currents associated with them that trap the convected fluid in a baroclinic vortex with cyclonic circulation near the surface and anticyclonic at depth. The horizontal scale, the buoyancy excess, and the magnitude of the currents that make up the plumes and cones are found to depend in a predictable way on the external parameters, B_0, f, and H.

Previous theoretical and modeling studies (e.g., Killworth 1976; Crépon et al. 1989; Madec et al. 1991) have parameterized the convective process and focused attention on the driving of a large-scale flow by it. Instead, here we set out to *resolve* localized sinking in a population of plumes (obviating the need for a parametric representation) and, simultaneously, the geostrophic adjustment and subsequent baroclinic instability of the resulting mixed column of convected water. To guide our numerical experiments we draw together and extend in section 3, scaling arguments due to Maxworthy and Narimousa (1993) and Fernando et al. (1991) inspired by their laboratory experiments of convection in the presence of rotation. In particular Maxworthy identifies a "natural" Rossby number for the system, Ro*, which depends only on the external parameters B_0, f, and H and is independent of values of molecular (and eddy) viscosities and thermal diffusivities. As in his laboratory experiments, Ro* turns out to be the controlling parameter of our numerical experiments. Indeed the present work can be regarded as a numerical analog of Maxworthy's laboratory study; each numerical experiment is characterized by a different Ro*. They are also reminiscent of the laboratory cylinder-collapse experiments of Saunders (1973), although here the surface buoyancy flux (rather than the buoyancy excess of the dense cylinder) is the controlled parameter. Our experiments are designed to elucidate the mechanism of open-ocean deep convection in a neutral (or near-neutral) ocean, attention being focused on the parameter regime most appropriate to the oceanic context. Studies of convection with rotation but in a stratified ocean are the subject of current research and will be reported later.

A very high-resolution nonhydrostatic convection model (~250 m in the horizontal and ~100 m in the vertical) is employed, based on the Boussinesq equations governing an incompressible fluid [see Brugge et al. (1991) for a detailed discussion of the numerical implementation of the model]. With it we explicitly simulate open-ocean deep convection driven by cooling at the sea surface, obviating the need for a parametric representation of convection. The model is described in section 4. In section 5 a series of numerical experiments is discussed in which Ro* is varied through two orders of magnitude; in each case the intensity and scale of the resulting convective motion, together with its geostrophically adjusted end state, are studied. For simplicity B_0 and H are kept constant and the rotation rate of the earth varied. The flux Rayleigh number

$$\mathrm{Ra}_f = \frac{B_0 H^4}{K_T^2 K_v},$$

where K_T is the (eddy) thermal diffusivity and K_v is the (eddy) viscosity, of our experiments is $\sim 10^9$ and the Taylor number

$$\mathrm{Ta} = \frac{f^2 H^4}{K_v^2}$$

ranges between 10^2 and 10^8, placing them, according to Boubnov and Golitsyn (1990), in the fully developed turbulence/geostrophic turbulence regime [see Fig. 1 of Fernando et al. (1991)]. This region of (Ra_f, Ta) space has also been studied numerically by Raasch and Etling (1991) but without specific application to the atmosphere or ocean. Due to finite availability of computer time and the very high resolution of the model, we can only model a small, doubly periodic patch of homogeneous ocean, of dimension 32 km square by 2 km deep. Within this patch, however, we are able to resolve localized sinking in a population of plumes scattered over the cooling region, each on a scale of about 1 km and, simultaneously, the geostrophic adjustment of the resulting mixed column of convected water and its subsequent fragmentation into coherent cones of cold fluid, which drift into the quiescent surroundings. We find that the behavior exhibited by the numerical simulations is well described by the scalings proposed.

2. Observational background

The MEDOC Group (1970) [see also the review by Killworth (1976)] identified three successive phases that characterize open-ocean deep convection: *preconditioning*, on the large scale (of order 100 km); *violent mixing* occurring in localized, intense plumes (on scales of order 1 km); and *sinking* and *spreading* of the convectively tainted water, on a scale of 5–10 km.

During *preconditioning*, the gyre-scale circulation and buoyancy forcing combine to predispose a particular site to overturn. For example, in the Gulf of Lions the background cyclonic circulation is subject to persistent surface heat loss priming the center of the gyre, where isopycnals dome up toward the surface. With the onset of strong surface forcing the near-surface stratification, over an area up to 100 km across, can be readily erased exposing the very weakly stratified water mass beneath to the surface (Swallow and Caston 1973). Subsequent cooling events can then initiate *violent mixing* in which the whole of the fluid column overturns, drawing buoyancy from depth, in numerous cells of horizontal scale of order 1 km; downward velocities of order 10 cm s^{-1} can develop in only a few hours (Stommel et al. 1971; Voorhis and Webb 1970) in this violent-mixing phase. The largest ascending and descending currents penetrate the whole depth of the mixed-water column. In concert the plumes are thought to rapidly mix properties over the preconditioned site, forming a "chimney" of homogeneous fluid. Chimneys ranging in scale from several to many tens of kilometers in width have been observed. At the density front between the homogeneous and stratified water, geostrophic eddies develop on a scale comparable with the local Rossby radius of deformation (L_ρ) of order 5 km in the MEDOC region (Gascard 1978; Sankey 1973). With the cessation of strong forcing there is a sharp decline in convective overturning; the predominantly vertical heat transfer of the mixing phase gives way to horizontal advection associated with eddying on geostrophic scales (Swallow and Caston 1973). The mixed fluid "slumps" under gravity and rotation, *spreading* out at middle depths and leading, on a time scale of days, to the disintegration of the chimney. As the dense fluid sinks, water from outside the chimney is drawn in, restratifying near-surface layers (Stommel 1972). In the event of a further mistral outbreak this stratified surface layer may once again be breached, deeply convecting plumes can develop, and the sequence of events is repeated.

Recently Schott and Leaman (1991) reported their detailed observations of a bout of violent mixing that occurred in almost neutral conditions. From the last week in January to the first in March 1987, instruments were deployed at the same preferred site of wintertime deep convection in the Gulf of Lions. An unusually early and severe mistral a fortnight before had already triggered deep convection there, the relic of which was a column of mixed water 2000-m deep, about 50 km across. Hydrographic sections through the quasi-homogeneous pool graphically emphasize the very weak stratifications that characterize an open-ocean deep-convection chimney. Inspection of σ_θ cross sections obtained at the very start of the observing period suggests that the vertical variation in σ_θ at the center of the patch over the depth of the mixed column (2000 m) is no more than 0.01 kg m^{-3}, implying a value of N^2 of less than 5×10^{-8} s^{-2}. Contemporaneous meteorological data indicates that the total surface heat loss, even allowing for likely airmass modification over the relatively warm sea, can exceed 850 W m^{-2} for a period of up to two days at the height of the storm.

A subsequent though less fierce mistral outbreak in mid-February reopened the erstwhile convection site. A renewed bout of violent mixing, sustained by a mean surface flux of 400 W m^{-2}, persisted for about a week. Negative buoyancy forcing, associated with the second mistral event, caused an enhancement of the surface density anomaly resulting in a progressive destabilization of the superficial layer of stratified water crowning the column, exposing the cold chimney beneath. Vertical velocity data obtained from an array of moored acoustic Doppler current profilers provide persuasive evidence for the development of convective plumes within the weakly stratified water. Over the entire depth range for which the profilers gave good data, between 100 m and 550 m, downwelling events in excess of 10 cm s^{-1} persisted for ~2 hours. From the estimated lateral translation time past a fixed mooring, plumes were estimated to have horizontal dimensions of around 1 km. Later, hydrographic sections reveal a reduction in temperature of the deepest water of 0.02 K, consistent with the mixing having distributed the effect of the surface forcing over the whole depth of the column. The velocity data also provides evidence of weaker upwelling, over a more extended area, in between the plume cores. Current-shear observations, between 20 and 1000 m, are consistent with the development of a net cyclonic circulation around the convective region. Large-amplitude meanders with length scales of about 10 km were observed on this front, possibly associated with baroclinic eddy development.

With the ebbing of the wind, vertical velocities declined sharply, their values falling back to 1 or 2 cm s^{-1}. Finally, restratification by intrusions of water from outside the site eventually blanketed the surface density anomaly.

3. Scaling for open-ocean deep convection

The purpose of the present study is to arrive at some understanding of the dynamics that control the overturning of an open-ocean convection chimney once violent mixing has commenced; accordingly attention is focused on deep-reaching convection in neutral (or almost neutral) conditions.

Before describing our numerical model and presenting simulations of open-ocean deep convection obtained using it, the conceptual model motivating our study and the physical ideas on which that model is based are presented. We are guided by the observations outlined in the previous section but also by laboratory experiments of thermal convection in the presence of rotation reviewed, for example, by Fernando et al. (1989).

a. Scaling ideas

We imagine that loss of buoyancy, associated with a sustained flux of magnitude B_0, at the surface of a homogeneous ocean of depth H, drives a thermal boundary layer of depth h as illustrated schematically in Fig. 1. In general, the depth h will be much smaller than the depth of the layer over which convective elements subsequently develop. Fluid from this boundary layer is evacuated to depth (and replenished from beneath by convectively unmodified water) by plumes, which for small times have a characteristic velocity scale

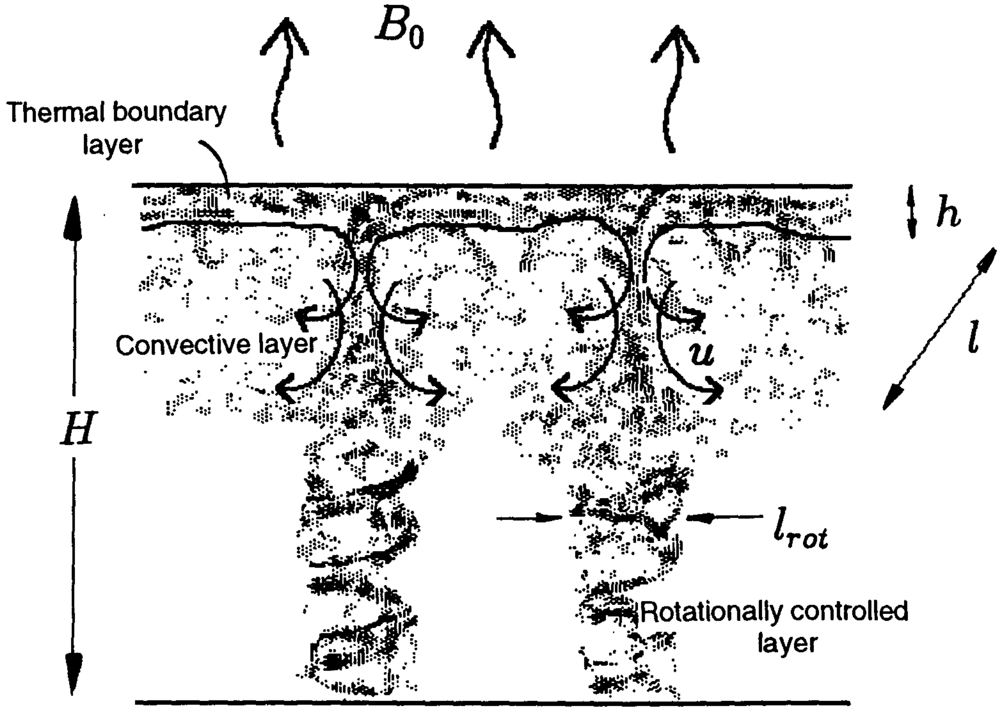

FIG. 1. A schematic representation of the "violent mixing" phase. A homogeneous ocean of depth H, exposed to surface negative buoyancy forcing B_0, responds through the development of a thermal boundary layer of depth h. From this layer intrusions of dense fluid—plumes—penetrate into the quiescent waters beneath having a characteristic length scale l and velocity scale u. These convective circulations sweep fluid out of the boundary layer to depth (and draw fluid up to the surface to be cooled) driving the convection layer below. If the ocean is sufficiently deep (as drawn here) then the convection layer will come under rotational control on the scale $l_{\rm rot} = (B_0/f^3)^{1/2}$.

u and space scale l with an aspect ratio $\sim$ unity. The plumes will evolve in time, penetrating into the fluid below, forming a convective layer that grows in time until it either extends down to the bottom of the ocean or comes under the influence of the earth's rotation.[2]

1) THERMAL BOUNDARY LAYER

We suppose that the boundary layer h is characterized by an (eddy) thermal diffusivity k that distributes the loss of buoyancy at the surface over its depth. This layer may be thought of as analogous to Howard's (1964) conductive layer (it will not be resolved in our numerical experiments). It grows diffusively with time at a rate controlled by k until it becomes statically unstable and releases negatively buoyant intrusions into the fluid beneath. These intrusions drive the convective layer below, setting up large-scale cells, plumes, that sweep fluid into and out of the boundary layer.

Now if we imagine that the buoyancy of the fluid parcels that make up the plumes are reset each time they pass through the thermal boundary layer, then the following scaling is suggested by the potential density equation:

$$\mathbf{u}\cdot\nabla\sigma \sim k\frac{\partial^2\sigma}{\partial z^2},$$

where $\mathbf{u} = (u, v, w)$ is the velocity in the horizontal (x, y) and vertical (z) directions, respectively, and σ is the potential density.

The preceding equation is a disjoint balance, diffusive processes becoming important only in the boundary layer. It suggests that

$$h \sim \left(\frac{kl}{u}\right)^{1/2} = l(\mathrm{Pe})^{-1/2}, \qquad (1)$$

where

$$\mathrm{Pe} = \frac{ul}{k} \qquad (2)$$

is a Peclet number for the potential density equation measuring the efficiency of transfer on the plume scale

---

[2] Here, we are considering sinking into a homogeneous fluid; in a stratified ocean the growth of the convective layer may also be affected by the ambient stratification.

relative to eddies in the thermal boundary layer at the surface. Rearranging Eq. (1) gives

$$\frac{h}{l} \sim \frac{1}{\sqrt{\mathrm{Pe}}}. \tag{3}$$

In the numerical experiments described later we assume that the thermal Peclet number is large (~ 100), that is, the plumes in the interior are much more efficient at transporting properties vertically than the convective (and in our numerical model, unresolved) elements comprising the surface thermal boundary layer. Thus, the boundary layer is shallow (~ 200 m) relative to the scale of the convective cells occupying the interior of depth ~ 2 km.

2) THE CONVECTION LAYER

We suppose that in the initial stages, plumes extending into the convective layer are so small in scale that they cannot feel the finite depth of the ocean H. Furthermore, if $t \leqslant f^{-1}$, then rotation is unimportant; only B_0 remains as the controlling parameter. It is then not possible to construct scales for the depth, buoyancy, or velocity of the plumes. The convective process must evolve in time, and we suppose that it proceeds in a self-similar way, as indicated in Fig. 1. From B_0,[3] and t the following scales can be formed:

$$\begin{aligned} l &\sim (B_0 t^3)^{1/2}, \\ u \sim w &\sim (B_0 t)^{1/2}, \\ g' &\sim \left(\frac{B_0}{t}\right)^{1/2}. \end{aligned} \tag{4}$$

Physical interpretation is aided if one uses the instantaneous l to eliminate t, yielding (e.g., Deardorff 1980) a velocity scale

$$u \sim w \sim (B_0 l)^{1/3} \tag{5}$$

and a reduced gravity

$$g' \sim \frac{B_0^{2/3}}{l^{1/3}}.$$

The preceding scalings can be readily understood. Consider a particle of fluid entering the thermal boundary layer of Fig. 1. The time a particle spends in the boundary layer is h/u, during which it will experience a forcing of magnitude B_0/h, so having its buoyancy changed by an amount

$$g' \sim \frac{B_0}{h} \times \frac{h}{u} = \frac{B_0}{u}.$$

As the negatively buoyant particle descends a distance l, it releases an amount of potential energy $\sim g'l$ and acquires kinetic energy $u^2 \sim w^2$, suggesting a velocity scale

$$u \sim w \sim (g'l)^{1/2}.$$

Combining these two equations, we arrive at the scalings (5) for u and g'.

Now we argue that as the scales l, u, and g' grow with time according to (4), they will become constrained either by the depth of the ocean or the earth's rotation. Let us consider each possibility in turn.

(i) *Scale constrained by the depth of ocean*

If it is the depth of the ocean that ultimately limits the scale of the cells then the following scalings are suggested by (5), independent of rotation

$$\begin{aligned} l &\sim l_{\mathrm{norot}} = H, \\ u &\sim u_{\mathrm{norot}} = (B_0 H)^{1/3}, \\ g' &\sim g'_{\mathrm{norot}} = \frac{B_0^{2/3}}{H^{1/3}}. \end{aligned} \tag{6}$$

The subscript "norot" indicates that these are the scales adopted in the absence of rotation.

(ii) *Scale constrained by the earth's rotation*

If the ocean is sufficiently deep, then the evolving convective layer will come under geostrophic control *before* it strikes the ocean bottom. In order for the sinking plumes to expand and deepen in time according to (4), they must "push" fluid aside. But lateral expansion will become increasingly difficult as the plumes reach scales at which rotation has imparted rigidity to the fluid column. The transition from 3D thermally driven plumes to quasi-2D rotationally dominated motions (represented schematically in Fig. 1) will occur as t approaches f^{-1} at which point, replacing t by f^{-1} in (4), the following scales pertain (see Maxworthy and Narimousa 1993; Fernando et al. 1991):

$$l \sim l_{\mathrm{rot}} = \frac{B_0^{1/2}}{f^{3/2}}, \tag{7}$$

$$u \sim u_{\mathrm{rot}} = \left(\frac{B_0}{f}\right)^{1/2}, \tag{8}$$

and

$$g' \sim g'_{\mathrm{rot}} = (B_0 f)^{1/2}, \tag{9}$$

where the subscript "rot" has been used to denote the scales at which rotation begins to be important.

It should be noted that the scales just identified are independent of assumptions concerning eddy viscosity and diffusivities; they are the velocity, space, and

---

[3] The units of buoyancy flux B_0 are $\mathrm{m}^2\,\mathrm{s}^{-3}$, a velocity multiplied by a reduced gravitational acceleration. In purely thermally driven convection, B_0 is related to the heat flux through Eq. (30).

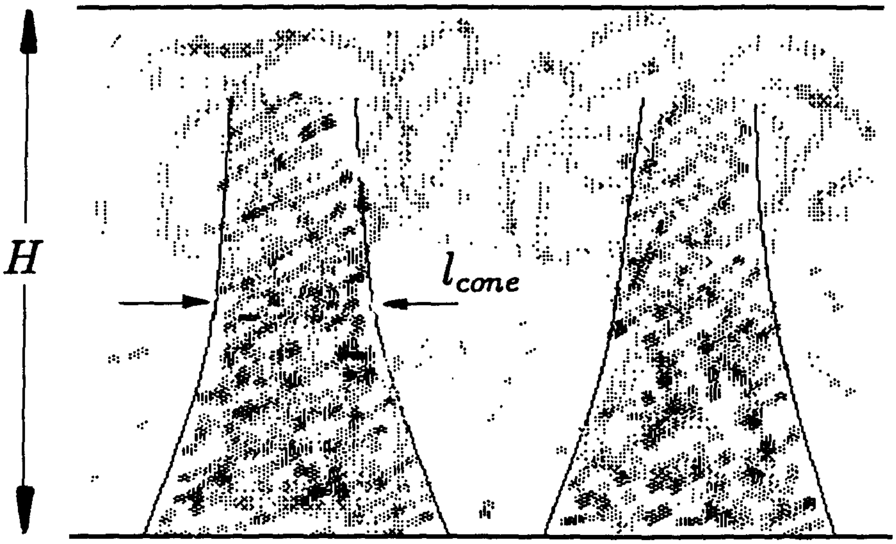

FIG. 2. A schematic representation of the earliest stages of the "sinking and spreading" phase. If $l_{\text{rot}} \ll H$, convectively modified waters, strongly under the influence of the earth's rotation, extend to the ocean bottom and "fill out" to the deformation radius l_ρ. "Cones" of spinning fluid are formed that trap the convected water and have a scale close to l_ρ.

buoyancy scales that can be constructed from the "external" parameters B_0, f, and H. At these scales the plume Rossby number is unity:

$$\mathrm{Ro} = \frac{u}{fl} \sim \frac{u_{\text{rot}}}{fl_{\text{rot}}} = 1. \qquad (10)$$

We see that as the limit $\mathrm{Ro} \sim 1$ is approached: (i) the time scale of the cells tends to the inertial period f^{-1}; (ii) the space scale of the cells approaches the radius of inertia u/f; (iii) the thermal boundary layer reaches a depth $(k/f)^{1/2}$—the distance the boundary layer can diffuse downwards in an inertial period, that is, the overturning time scale of the plumes responsible for eroding it. It is interesting that the scale $(k/f)^{1/2}$ resembles that of an Ekman layer, although here it is a thermally driven layer with rather different physics; it is the overturning time scale outside the boundary layer that sets the depth scale; and (iv) the convective layer reaches down a distance that scales like l_{rot}, below which the motion will be quasi-two dimensional and dominated by rotation.

3) THE GEOSTROPHICALLY ADJUSTED END STATE

Maxworthy and Narimousa (1993) argue, guided by laboratory experiments, that if the depth of the ocean $H \geqslant l_{\text{rot}}$, the scale at which rotation becomes important, then the convective process proceeds through the development of cones of geostrophically adjusted fluid that extend down from the rotationally dominated convective layer, as illustrated schematically in Fig. 2, until they reach the bottom of the ocean. The scale of these spinning cones of dense fluid is imagined to initially match that of the eddies of scale l_{rot} above, but as they extend down to the bottom they fill out to the deformation radius l_ρ based on g'_{rot}, H, and f. Thus, Maxworthy suggests that the end state of the convective process consists of geostrophically adjusted cones of fluid having a scale

$$l_{\text{cone}} \sim l_\rho = \frac{\sqrt{g'_{\text{rot}}H}}{f} = \frac{B_0^{1/4}H^{1/2}}{f^{3/4}}. \qquad (11)$$

The aspect ratio of the cones of dense fluid l_{cone}/H scales with the (square root of the) natural Rossby number of the system because

$$\frac{l_{\text{cone}}}{H} \sim \frac{l_\rho}{H} = \frac{1}{f}\left(\frac{g'_{\text{rot}}}{H}\right)^{1/2} = \frac{B_0^{1/4}}{f^{3/4}H^{1/2}} = \sqrt{\mathrm{Ro}^*}. \qquad (12)$$

Here the parameter Ro^*, depending only on external parameters, is a Rossby number formed from scales H, f, and u_{rot}:[4]

$$\mathrm{Ro}^* = \frac{u_{\text{rot}}}{fH} = \frac{g'_{\text{rot}}}{f^2H} = \frac{B_0^{1/2}}{f^{3/2}H}. \qquad (13)$$

It is a measure of the slope of the front between the convected and ambient water at the edge of the cone.

---

[4] Stern et al. (1982) call the parameter $f^{-2}g'_{\text{rot}}/H$ a hydrostatic number; it is normally large in geophysical systems in which the depth of the fluid is small relative to the deformation radius. In the hydrostatic limit it disappears as a parameter. Here, however, Ro^* can be small.

The square of Ro* can also be thought of as a measure of the intensity of the buoyancy forcing.

The foregoing scaling provides a compelling framework in which to conduct a series of numerical experiments enquiring into open-ocean deep convection, its intensity, and scale. But first, guided by the observations, we estimate typical magnitudes of the key parameters identified above for the open-ocean deep convection regime.

b. Oceanographic parameters

Table 1 presents velocity, buoyancy, and space scalings, together with Ro* as a function of B_0 (corresponding to a heat loss ranging from 100 to 1500 W m^{-2}). We have assumed that $H = 2$ km and $f = 10^{-4}$ s^{-1}. In the vigorous convective regime, if the scaling is appropriate, we might expect to find velocities of ~5–10 cm s^{-1} with rotational effects becoming important on scales $\leqslant 1$ km, broadly in accord with the observations reviewed in section 2. We see that for parameters typical of open-ocean deep convection Ro* $\leqslant 1$, $l_{\text{rot}}/H \leqslant 1$; so rotation is likely to play an important role. This is indeed borne out by our numerical experiments described in section 5.

4. A nonhydrostatic ocean model

To explicitly model motions on the scale of convective plumes, a nonhydrostatic model with rotation effects included must be employed. Conventional primitive equation ocean models assume precise hydrostatic balance between the pressure and the density fields. The condition, however, for the validity of the hydrostatic approximation is (there are some subtleties that are explored in appendix A)

$$\frac{H^2}{l^2} \ll 1, \tag{14}$$

where H and l are, respectively, the scales of the motion system in the vertical and the horizontal. Thus, in the deep convection regime, nonhydrostatic effects become important on horizontal scales comparable to the local ocean depth, ~1 to 2 km. It would seem important then that in attempting to explicitly model convection on the plume scale, nonhydrostatic effects should be adequately represented. Accordingly, in the explicit simulations of deep convection presented in section 5, a fully nonhydrostatic convection model has been used. The model, in its continuous and finite-difference form, is described in detail in Brugge et al. (1991) and Brugge and Marshall (1991), where its connection with Miller's (1974) compressible atmospheric mesoscale model, on which it is based, is clarified. It is a second-order, finite-difference model on a C grid employing an Euler backward time-stepping scheme. We do not restate those details here, but for completeness the continuous equations—the Boussinesq equations in the presence of rotation—that form the basis of the model are now set out.

a. The continuous equations

The nonhydrostatic equations for a Boussinesq incompressible fluid with an equation of state appropriate to seawater, on which the model is based, are in height coordinates

$$\left.\begin{aligned} \frac{Du}{Dt} + \frac{1}{\rho_0}\frac{\partial p'}{\partial x} - fv &= F_u - D_u \\ \frac{Dv}{Dt} + \frac{1}{\rho_0}\frac{\partial p'}{\partial y} + fu &= F_v - D_v \end{aligned}\right\}, \tag{15}$$

TABLE 1. $H = 2$ km, $f = 1 \times 10^{-4}$ s^{-1}. Velocity and space scales suggested by our scaling in the open-ocean deep convection regime.

		Q (W m^{-2})			
		100	500	1000	1500
		B_o (m^2 s^{-3})			
Scaling		5.00×10^{-8}	2.25×10^{-7}	5.00×10^{-7}	7.25×10^{-7}
l_{rot} (km)	$\left(\frac{B_o}{f^3}\right)^{1/2}$	0.22	0.47	0.71	0.85
u_{rot} (m s^{-1})	$\left(\frac{B_o}{f}\right)^{1/2}$	0.02	0.05	0.07	0.09
l_p (km)	$\frac{B_o^{1/4}H^{1/2}}{f^{3/4}}$	0.67	0.97	1.19	1.31
Ro*	$\frac{B_o^{1/2}}{f^{3/2}H}$	0.11	0.24	0.35	0.43
Ro*$^{1/2}$	$\frac{B_o^{1/4}}{f^{3/4}H^{1/2}}$	0.33	0.49	0.59	0.65

$$\frac{Dw}{Dt} + g\frac{\rho'}{\rho_0} + \frac{1}{\rho_0}\frac{\partial p'}{\partial z} = F_w - D_w, \qquad (16)$$

$$\frac{\partial u}{\partial x} + \frac{\partial v}{\partial y} + \frac{\partial w}{\partial z} = 0, \qquad (17)$$

$$\frac{DT}{Dt} = F_T - D_T, \qquad (18)$$

$$\frac{DS}{Dt} = F_S - D_S, \qquad (19)$$

where

$$\frac{D}{Dt} = \frac{\partial}{\partial t} + u\frac{\partial}{\partial x} + v\frac{\partial}{\partial y} + w\frac{\partial}{\partial z} \qquad (20)$$

is the substantial derivative. Here, S is the salinity, T[5] the temperature, and

$$\rho = \rho(T, S, z) \qquad (21)$$

is an appropriate equation of state; ρ_0 is a standard constant value of density and ρ' the perturbation of ρ from the initial density profile (ρ_s) in hydrostatic balance with the pressure field (p_s). The deviation of the pressure from p_s is p'. The velocity in the three coordinate directions—x pointing east, y pointing north, and z vertically—are u, v, and w, respectively. Note that the momentum equations include Coriolis terms with a constant Coriolis parameter (f). Forcing and dissipation are represented symbolically, with an appropriate subscript, by F and D. A schematic diagram of the model configuration is presented Fig. 3.

For completeness a salinity variable S is included in the model description together with its prognostic equation and a generalized statement of the equation of state. In the series of experiments presented later, however, we carry no salinity variable, and a highly idealized equation of state is employed in which ρ is a linear function of temperature (see section 4b).

SUBGRID-SCALE PARAMETERIZATIONS AND BOUNDARY CONDITIONS

The choice of subgrid-scale parameterization depends on the use to which the model is to be put but also, particularly where dissipative processes are to be represented, on one's taste and prejudice. Various more or less sophisticated dissipative parameterizations have been used, but in the present experiments a standard Fickian form has been adopted for D on the right-hand side of the momentum and thermodynamic equations (15), (16), and (18):

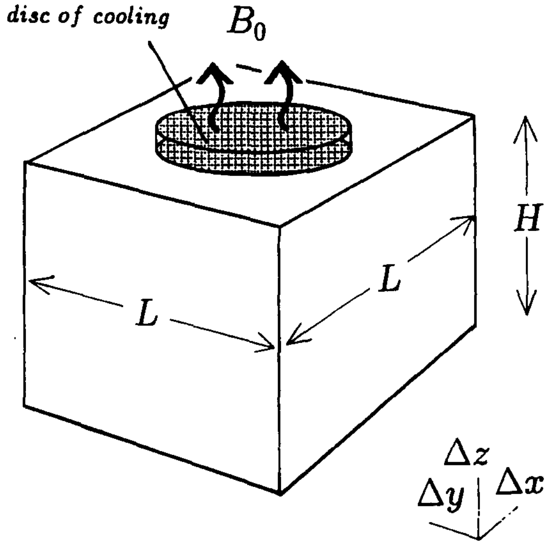

FIG. 3. A schematic representation of the numerical model configuration. All simulations were carried out in a doubly periodic box 32 km square ($L_x = L_y = 32$ km) by 2 km deep ($H = 2$ km) on a $132 \times 132 \times 19$ grid ($\Delta X = \Delta Y = 250$ m, $\Delta Z = 100$ m). Convection is induced over a disk of radius r, depth h, by the application of a localized buoyancy forcing B_0.

$$D_\Phi = -K_\Phi^h\left(\frac{\partial^2\Phi}{\partial x^2} + \frac{\partial^2\Phi}{\partial y^2}\right) - K_\Phi^v\frac{\partial^2\Phi}{\partial z^2}. \qquad (22)$$

Here K_Φ^h and K_Φ^v are horizontal and vertical diffusion coefficients for the quantity Φ where Φ may be T, u, v, or w. They are assumed to be positive and held constant in time and space.

The K should be interpreted as eddy diffusivities and viscosities representing the turbulent transfer of properties on scales that are not resolved by the grid. As in all numerical models, however, these terms are to some extent ad hoc and multipurpose, being used partly as a computational device to suppress spurious noise, but also representing physical processes that cannot be resolved in the model. The Laplacian form (22) was chosen for its simplicity but also to facilitate analytic study of the stability of a background stratification (see section 6 and appendix B). It is important to emphasize, however, as will become clear in section 5, the key results of our study, which concern the velocity and space scales of the geostrophically adjusted end state of deep convection, are entirely independent of the K provided, of course, they remain sufficiently small.

At the lateral boundaries of our model we adopt periodic boundary conditions; this obviates the need for higher-order conditions or the resolution of frictional boundary layers there.

To eliminate fast-moving surface gravity waves at the upper boundary of our model we apply the rigid-lid condition

---

[5] If required, the effects of compressibility can be conveniently accommodated by replacing T in Eq. (21) with potential temperature (θ) and in place of (18) integrating a prognostic equation forward for θ. An equation of state of the form $\rho = \rho(\theta, S, z)$ is then employed.

$$w = 0 \quad \text{at} \quad z = 0. \tag{23}$$

Likewise, at the flat lower boundary of the model we set

$$w = 0 \quad \text{at} \quad z = -H. \tag{24}$$

Furthermore, we assume that the upper and lower boundaries of the model are "free," setting the second derivative of w to zero

$$\frac{\partial^2 w}{\partial z^2} = 0 \quad \text{at} \quad z = 0, -H. \tag{25}$$

The Fickian diffusion terms necessitate the use of additional boundary conditions at the top and bottom of the model. We choose to set the vertical flux of horizontal momentum and heat to zero

$$\frac{\partial \Phi}{\partial z} = 0, \tag{26}$$

where Φ is T, u, or v. These ensure that, in toto, momentum and heat are conserved in the periodic model in the absence of imposed sources and sinks.

b. Model setup

1) INITIAL STATE AND BUOYANCY FORCING

Our model is initialized with a homogeneous, resting ocean governed by an equation of state of the following form:

$$\rho = \rho_0[1 - \epsilon(T - T_0)], \tag{27}$$

where ϵ is the coefficient of thermal expansion of water (taken to be $2 \times 10^{-4}\ \mathrm{K}^{-1}$) with ρ_0 and T_0 appropriately chosen constants. In the simulations presented here, the model does not contain any salt.

Buoyancy loss is affected by subtracting a decrement of temperature from the body of the fluid in a surface boundary layer, the numerical analog of the thermal boundary layer discussed in section 3a(1), at a rate given by the function $F_T(x, y, z, t)$ in the thermodynamic equation (18). All other forcing functions are set to zero. The function F_T is employed to trigger convection in the surface layers of the model; it represents the net thermodynamic effect of unresolved convective motions that distribute the cooling, induced by heat loss at the surface, over the thermal boundary layer.

Here F_T has been chosen to have the form

$$F_T = \mathcal{F}(z) \times \mathcal{G}(x, y) \times \mathcal{T}(t), \tag{28}$$

where, respectively, $\mathcal{F}$, $\mathcal{G}$, and $\mathcal{T}$ specify the vertical, horizontal, and temporal dependence of the forcing. The $\mathcal{F}$ is related to heat flux ($\mathcal{H}$) through the ocean's surface by

$$\left.\begin{aligned} \mathcal{F} &= \mathcal{H}/\rho_0 C_w h && \text{for} \quad -h < z \leqslant 0 \\ \mathcal{F} &= 0 && \text{for} \quad -H \leqslant z \leqslant -h \end{aligned}\right\}, \tag{29}$$

where $\mathcal{H}$ is in watts per square meter, C_w is the specific heat of water, ρ_0 the mean density of seawater, and h the depth over which $\mathcal{F}$ is applied. Note that buoyancy flux through the sea surface is related to the heat flux through

$$B_0 = \frac{g\epsilon\mathcal{H}}{\rho C_w}, \tag{30}$$

where $C_w = 3900\ \mathrm{J\ kg^{-1}\ K^{-1}}$ is the specific heat of water.

We identify h with the depth of the thermal boundary layer in the scaling analysis of section 3; the convective layer will be resolved. The form of (29) assumes that the unresolved motions in the near-surface layer "instantaneously" distribute the effect of the surface cooling over depth. It is important to appreciate that setting h is equivalent to prescribing the magnitude of k, the eddy thermal diffusivity in the boundary layer because, matching the buoyancy flux at the sea surface to vertical eddy transfer

$$B_0 \sim \frac{kg'}{h},$$

suggesting, appropriately, $k \sim B_0 h/g' = h(B_0 l)^{1/3} = hu$, [using Eq. (4) and (5)] a vertical eddy scale multiplied by a velocity scale.

2) DOMAIN, MODEL RESOLUTION, AND DIFFUSION COEFFICIENTS

In the experiments presented here we choose

$$\mathcal{H} = 800\ \mathrm{Wm^{-2}},$$

$$L_x = L_y = 32\ \mathrm{km},$$

$$h = 200\ \mathrm{m}, \quad H = 2\ \mathrm{km}.$$

We cool over a circular patch that has a radius very much larger than the radius of deformation, which subsequently develops in response to the cooling, but we retain the high spatial resolution necessary to simultaneously resolve motions on the scale of the plumes themselves. Due to the very small horizontal scale of the convective plumes this is a highly demanding and costly computational task, requiring a compromise between spatial resolution and the size of the domain that can be represented in the model. This compromise was reached by choosing a [section 4b(1)] $\mathcal{G}(x, y)$ that applies cooling over a circular patch of radius 8 km in the center of the doubly periodic domain of 32 km square by 2 km deep (see Fig. 3). The (uniform) resolution of the model in all cases is $\Delta x = \Delta y = 250$ m and $\Delta z = 100$ m. A decrement of temperature is applied to the model of a magnitude given by Eq. (29) at the uppermost two thermodynamic levels of the model (at depths of 50 m and 150 m).

Our choice of $\mathcal{G}(x, y)$ can be thought of as a crude parameterization of preconditioning, since it very effectively confines the convective overturning in the model to the disk of cooling. Use of this localized patch of cooling also permits the convectively modified waters formed beneath the cooling region to escape and geostrophically adjust in the surrounding fluid. One of the main foci of attention in section 5 will be the scale of the fragments of geostrophically adjusted fluid that coalesce in these quiescent regions surrounding the forced disk.

The following values of eddy viscosity and thermal diffusivity were used in all experiments: $K^h = 5\ \mathrm{m}^2\ \mathrm{s}^{-1}$ and $K^v = 0.2\ \mathrm{m}^2\ \mathrm{s}^{-1}$. Diffusivities for heat and momentum were chosen to be the same because, a priori, we have no reason to expect them to be different. Interpreted in terms of a mixing-length hypothesis, a magnitude of $5\ \mathrm{m}^2\ \mathrm{s}^{-1}$ is consistent with an eddy velocity of $2\ \mathrm{cm\ s}^{-1}$ correlated over a space scale of 250 m, the horizontal resolution of the model. A very much smaller level of vertical diffusion was employed to ensure that advection—that is, resolved convection—rather than diffusion, is the agency by which information travels vertically in the model. In a time t, boundary conditions at the surface are diffused vertically by the explicit diffusion a distance $\sqrt{\pi K^v t}$ into the interior of the fluid. Thus, for a K^v of $0.2\ \mathrm{m}^2\ \mathrm{s}^{-1}$ information is diffused to a depth of only 100 m in 6 hours (one grid length), a reassuringly small distance.

One day of integration on the $132 \times 132 \times 19$ grid, using a time step of 60 seconds, requires 90 minutes of a single CRAY-XMP processor and 5 million words of memory.

5. Numerical simulations of convective overturning and geostrophic adjustment in a rotating neutral ocean

To investigate the relevance of the scaling discussed in section 3 we present results from a series of numerical experiments in which Ro* is varied by two orders of magnitude about a reference simulation in which

$$B_0 = 4 \times 10^{-7}\ \mathrm{m}^2\ \mathrm{s}^{-3}, \quad f = 10^{-4}\ \mathrm{s}^{-1}, \quad H = 2\ \mathrm{km}$$

(corresponding to a heat loss of $800\ \mathrm{W\ m}^{-2}$).

The implied flux Rayleigh number ($\mathrm{Ra}_f = B_0 H^4 / K^{v3}$) is 8×10^8 and the Taylor number ($\mathrm{Ta} = f^2 H^4 / K^{v2}$) ranges between 4×10^2 and 10^8, placing our experiments in the fully developed turbulence/geostrophic turbulence regime [regions 3 and 4 of Fig. 1 of Fernando et al. (1991)].

Unless otherwise stated, cooling was applied for a two-day period over a 16-km disk, after which time it was set to zero and the model ocean allowed to geostrophically adjust.

The change in Ro* is brought about by varying the rotation rate of the earth. Table 2 presents u_{rot}, l_{rot}, and Ro* for the experiments described here. We categorize our experiments as high rotation if $l_{\mathrm{rot}} \leqslant H$ with $\mathrm{Ro}^* \leqslant 1$ and low rotation if $l_{\mathrm{rot}} \geqslant H$ with $\mathrm{Ro}^* \geqslant 1$. The table suggests that rotation ought to have an important influence in the reference experiment where $f = 10^{-4}\ \mathrm{s}^{-1}$, have a lesser influence at lower rotation rates, and dominate at higher rotation rates. By comparing with Table 1 we see that the high-rotation experiments are the most relevant to the open-ocean deep convection regime since here Ro* is considerably less than one.

a. High rotation

1) PLUMES

In response to the applied cooling, a "reservoir" of dense water forms as a surface thermal boundary layer of depth $h = 200$ m which, by 6 hours, satisfies a Rayleigh criterion based on the depth of the boundary layer

TABLE 2. The numerical experiments: $B_o = 4 \times 10^{-7}\ \mathrm{m}^2\ \mathrm{s}^{-3} \equiv 800\ \mathrm{W\ m}^{-2}$, $H = 2$ km.

Scaling	f ($\times 10^{-4}$) (s^{-1})	0.01	0.20	0.50	0.80	1.00	2.00	3.00	5.00
		Low rotation		High rotation					
l_{rot} (km)	$\left(\frac{B_o}{f^3}\right)^{1/2}$	632.46	7.07	1.79	0.88	0.63	0.22	0.12	0.06
u_{rot} ($\mathrm{m\ s}^{-1}$)	$\left(\frac{B_o}{f}\right)^{1/2}$	0.63	0.14	0.09	0.07	0.06	0.05	0.04	0.03
l_p (km)	$\frac{B_o^{1/4} H^{1/2}}{f^{3/4}}$	35.57	3.76	1.89	1.33	1.13	0.67	0.49	0.34
Ro*	$\frac{B_o^{1/2}}{f^{3/2} HJ}$	316.23	3.54	0.89	0.44	0.32	0.11	0.06	0.03
$\mathrm{Ro}^{*\,1/2}$	$\frac{B_o^{1/4}}{f^{3/4} H^{1/2}}$	17.78	1.88	0.94	0.66	0.57	0.33	0.25	0.17

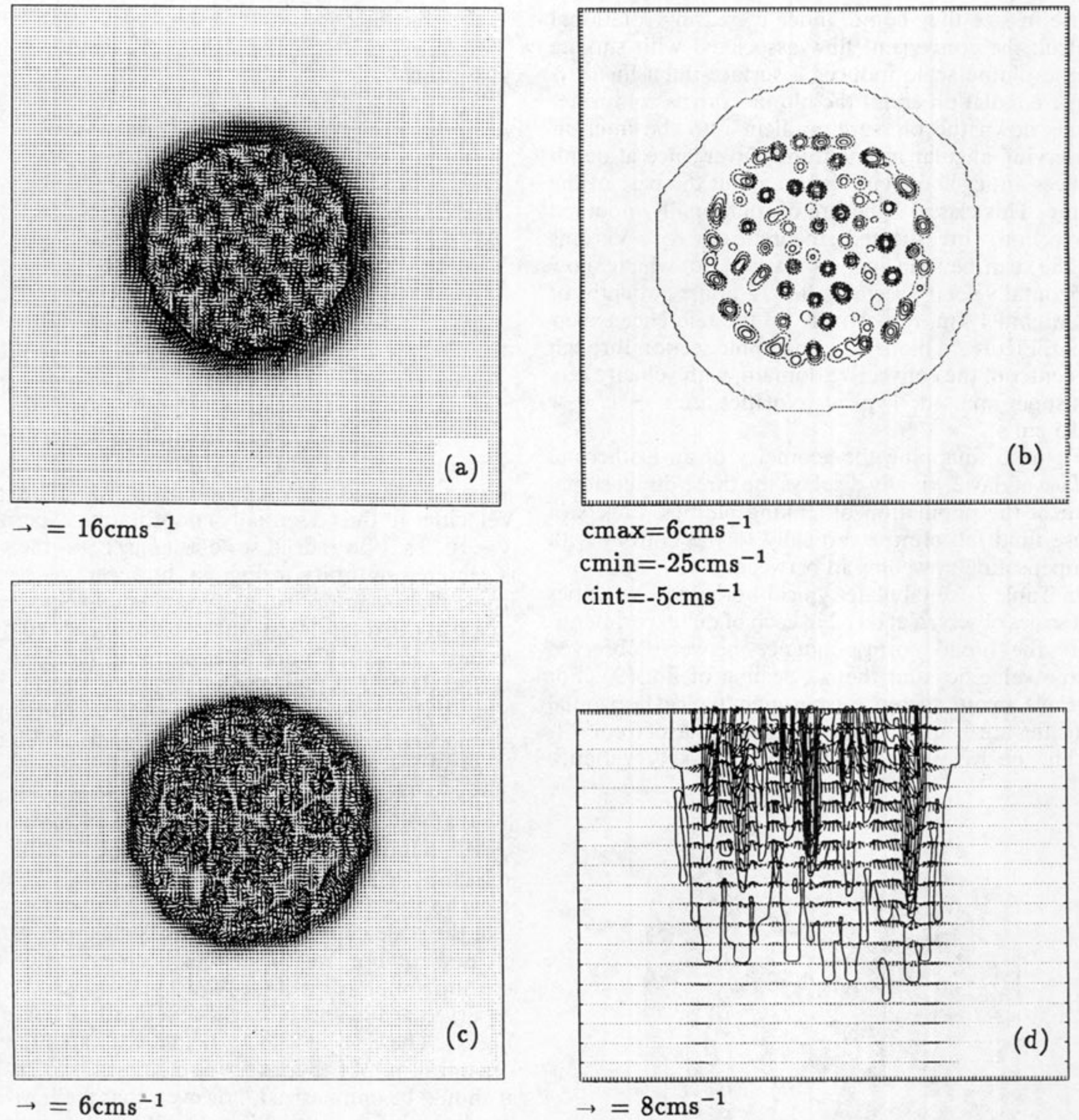

FIG. 4. The reference simulation at 12 hours. (a) The pattern of horizontal currents at 200 m over the 32 km square, doubly periodic domain. Arrows are plotted at each grid point of the model; $u_{\max} = 16$ cm s^{-1}. (b) The pattern of vertical velocity over the domain at a depth of 1 km. The contour interval is 5 cm s^{-1} with thick contours indicating downward motion. The dashed line is the zero contour. The ticks, every 250 m, indicate the horizontal resolution of the model. (c) The pattern of horizontal currents at 1 km; $u_{\max} = 6$ cm s^{-1}. (d) An east–west section through the middle of the developing chimney showing temperature contours and the velocity field in the plane of the section. The contour interval is 0.01 K. The ticks indicate the horizontal (250 m) and vertical (100 m) resolution of the model; $u_{\max} = 8$ cm s^{-1}.

and becomes statically unstable (see section 6a). The ensuing overturning takes the form of numerous narrow plumes of scale ~ 1 km which, while the cooling persists, penetrate progressively deeper into the interior, lowering the mean base of the convective layer and, in time, distributing the influence of intense surface heat loss over the whole depth of the ocean. Figure 4b shows the vertical velocity at 1 km after 12 hours in the reference experiment. Although small, these downwelling regions, peppering the convection site, are resolved by the finite-difference grid; see the tick marks in the figures indicating the resolution of the model.

After one day, convective circulations convey dense fluid from the surface boundary layer right down to the bottom and bring less dense water up, to be cooled at the surface. As individual plumes mature and increase in size they come under increasing rotational control; the convergent flow associated with sinking on the plume scale induces a surface-intensified cyclonic circulation about the plume core as cold water spirals down the pressure gradient into the interior, conserving angular momentum. Divergence at depth induces anticyclonic circulation about the base of the plume. This classic signature of rotationally modified convection, investigated theoretically by Veronis (1958), can be seen in Figs. 4a and 4c, which show horizontal velocity vectors after 12 hours at depths of 200 m and 1 km, respectively, in the reference experiment. Figure 4d plots a hydrographic section through the center of the convective domain, with velocity vectors superimposed. Typical velocities are $u \sim v \sim w \sim 15$ cm s^{-1}.

Figure 5, mapping the geometry of an isothermal surface at day 2, vividly displays the three-dimensional form of the population of sinking plumes; fingers of dense fluid fall almost vertically to the bottom with compensating upwelling in between.

In Table 3 we tabulate typical horizontal velocities and scales observed at day 2 in each of our experiments. Note the broad correspondence between observed plume velocities and the $u_{\rm rot}$ scaling of Eq. (9). For example, in our reference experiment typical horizontal velocities are 5 cm s^{-1}, close to the $u_{\rm rot}$ scale of 6 cm s^{-1}. In Fig. 6a we plot the horizontal velocity variance $(\overline{u'^2 + v'^2})^{1/2}$ at day 2 as a function of depth over the convective disk for our experiments, normalized with respect to the nonrotating scaling $(B_0H)^{1/3}$ [Eq. (6)]. Velocities in the (essentially) nonrotating experiment $f = 10^{-6}$ s^{-1} do indeed scale as $(B_0H)^{1/3}$—the curve is centered on unity in Fig. 6a; however, we see that in the high-rotation regime typical eddy velocities decrease as the rotation rate increases as suggested by the scaling, Eq. (9). Figure 6b again plots $(\overline{u'^2 + v'^2})^{1/2}$ against depth but now normalized with respect to $u_{\rm rot}$ [Eq. (9)], while in Fig. 6c it is plotted against depth normalized by $l_{\rm rot}$ [Eq. (8)]. The normalized velocities from all the high-rotation experiments collapse onto the same line centered around unity, strongly suggesting that $(B_0/f)^{1/2}$ is indeed the velocity scale adopted by the plumes. Note that it is only the $f = 10^{-6}$ s^{-1} velocities that appear anomalous when scaled with respect to the rotational velocity $u_{\rm rot}$. Table 3 suggests that the scale chosen by the plumes collapses with increased rotation rate; $l_{\rm plume}$ has been estimated from the horizontal scales of the model vertical velocity field observed at the end of day 2 at a depth of 1 km (see Fig. 7). The vertical velocity field reveals an interesting organization of the convective elements into "rolls."[6] It should be emphasized, however, that the horizontal resolution of the model is only 250 m. The finite resolution of the model and eddy viscosity on the grid scale must have a very significant effect on scale and organization of the plumes, particularly at high rotation rates. From Table 2, we observe that $l_{\rm rot}$ is only 60 m for our chosen parameters when $f = 5 \times 10^{-4}$ s^{-1}. Given that our model is barely resolving the scale collapse at high rotation, it is remarkable that the velocity scaling evident in Fig. 6 appears to still be captured in the model.

TABLE 3. Horizontal plume velocities and scales observed at day 2 at a depth of 1 km.

$f(\times 10^4)$ (s^{-1})	$u_{\rm plume}$ (m s^{-1})	$u_{\rm rot}$ (m s^{-1})	$l_{\rm plume}$ (km)	Ro$_{\rm plume}$
0.01	0.10	0.63	—	—
0.20	0.14	0.14	1.54	4.45
0.50	0.07	0.09	1.35	0.98
0.80	0.06	0.08	1.25	0.61
1.00	0.05	0.06	1.06	0.51
2.00	0.03	0.05	0.87	0.27
3.00	0.04	0.04	0.77	0.17
5.00	0.03	0.03	0.67	0.10

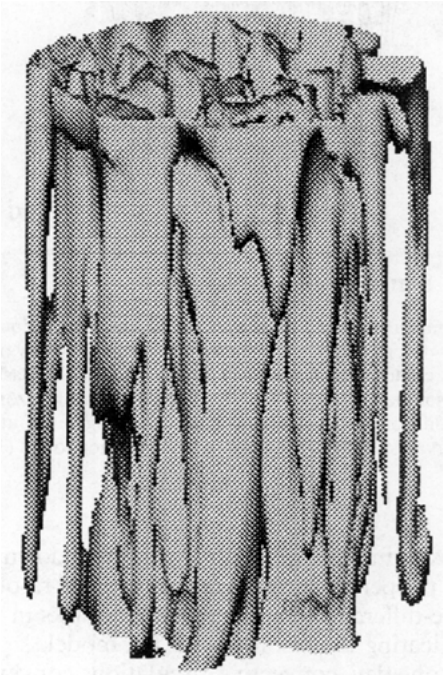

FIG. 5. An isothermal surface from the reference experiment at the end of day 2 capturing the 3D form of the population of sinking plumes.

---

[6] One possible explanation is that the cells orient themselves into rolls that are transverse to the large-scale shear (that they themselves drive); however, close study of the model fields does not support this idea.

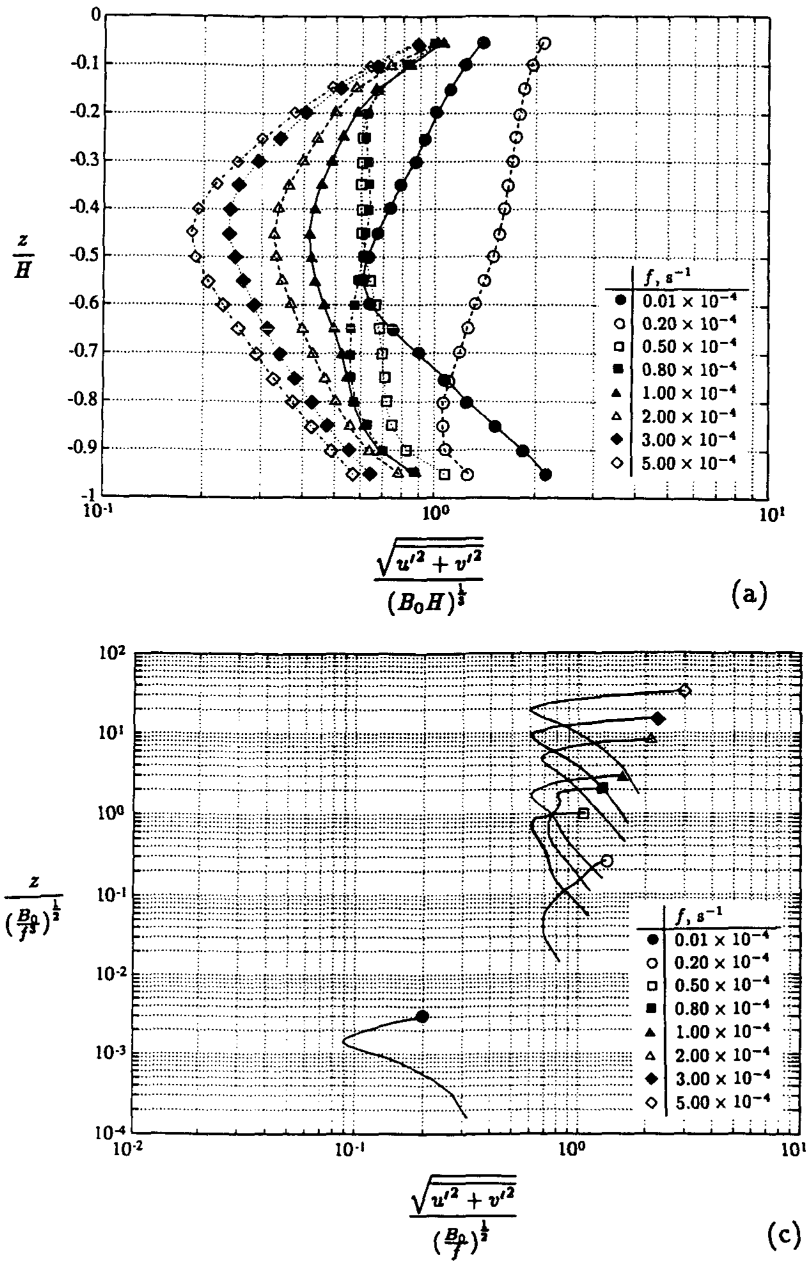

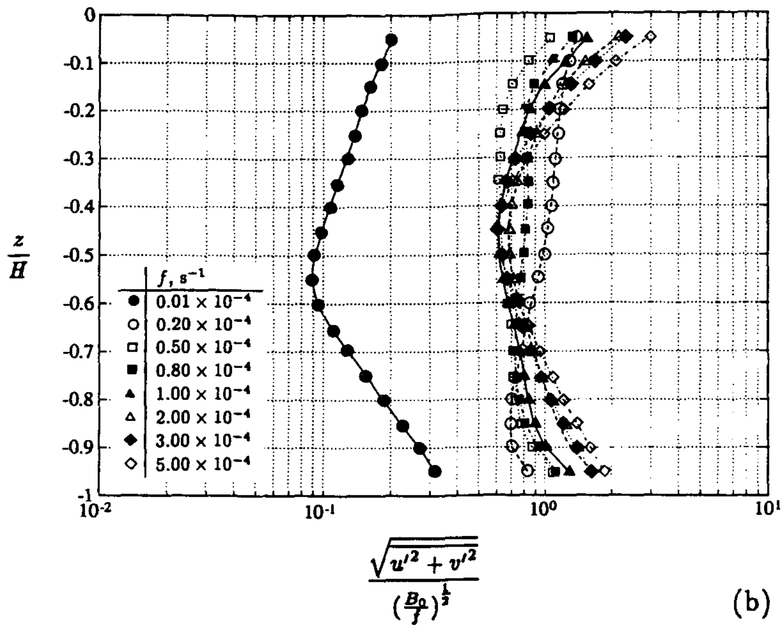

FIG. 6. Horizontal velocity variance $(\overline{u'^2 + v'^2})^{1/2}$: (a) normalized with respect to the nonrotating scaling $(B_0H)^{1/3}$ and plotted as a function of depth over the convective disk, (b) normalized with respect to u_{rot} and plotted as a function of depth, and (c) normalized with respect to u_{rot} and plotted against depth normalized with respect to l_{rot}.

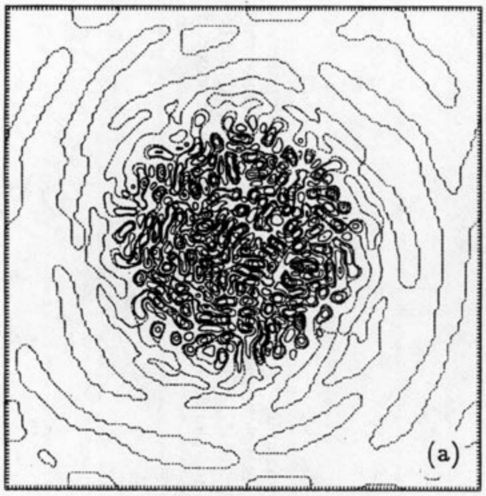

cmax=9cms^{-1},cmin=-9cms^{-1},cint=2cms^{-1}

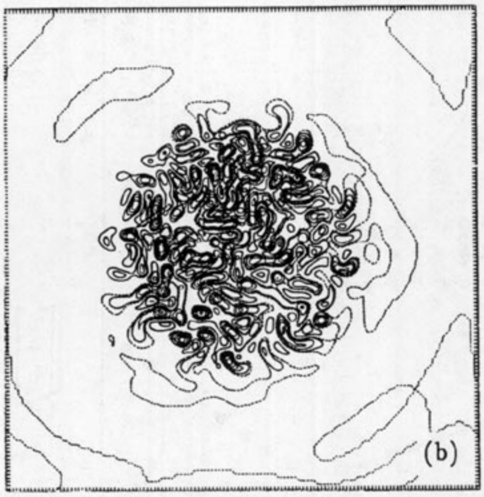

cmax=9cms^{-1},cmin=-14cms^{-1},cint=2cms^{-1}

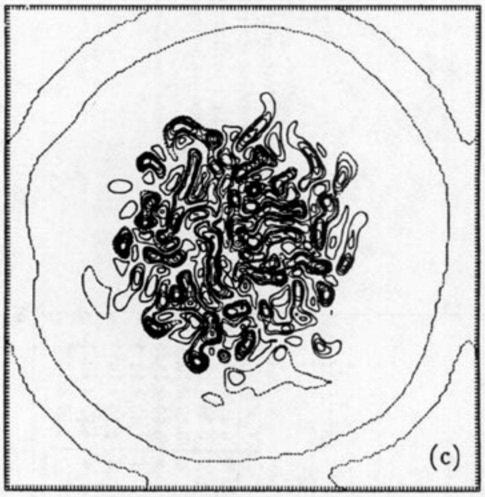

cmax=11cms^{-1},cmin=-13cms^{-1},cint=2cms^{-1}

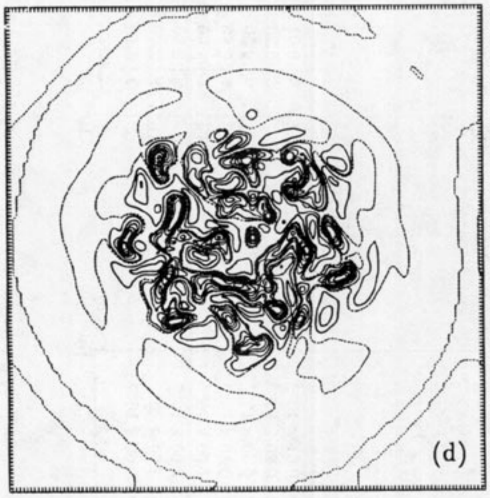

cmax=9cms^{-1},cmin=-18cms^{-1},cint=2cms^{-1}

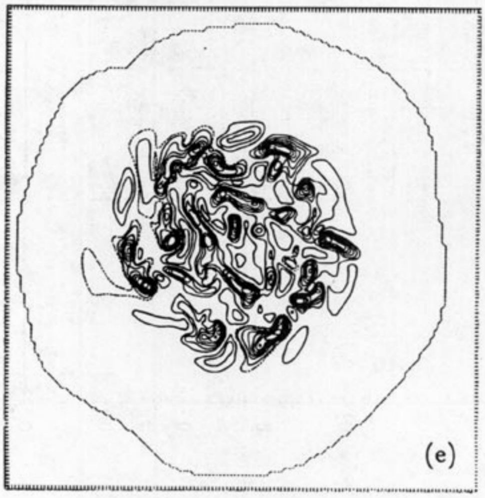

cmax=9cms^{-1},cmin=-19cms^{-1},cint=2cms^{-1}

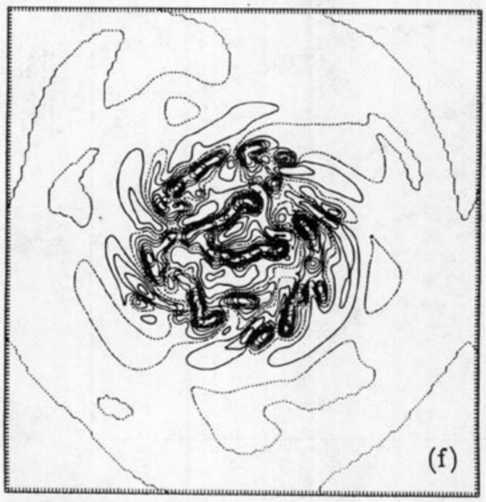

cmax=10cms^{-1},cmin=-21cms^{-1},cint=2cms^{-1}

The plume Rossby number

$$\mathrm{Ro}_{\mathrm{plume}} = (\overline{u'^2 + v'^2})^{1/2}/fl_{\mathrm{plume}}$$

in Table 3 suggests that rotation is important in controlling the dynamics of the plumes. Our model indicates, however, that the plumes are three dimensional with strong vertical velocities approaching horizontal current speeds; they are modified but not dominated by rotation, even at high rotation rates. Indeed, it is only on the cessation of cooling that vertical velocities subside and geostrophically balanced motions predominate.

A central tenet of the scaling arguments presented in section 3 is that if $l_{\mathrm{rot}} \leqslant H$, as in the high-rotation experiments, then vertical scales in the convection layer will be proportional to l_{rot}, rather than H. One consequence of this is that the buoyancy excess in the falling plumes ought to scale like $\sqrt{B_0 f}$ independent of H [see Eq. (9)]. Furthermore, we would not expect properties to be well mixed on all scales over the depth of the ocean if $l_{\mathrm{rot}} \leqslant H$. The systematic effect of rotation on the buoyancy of the plumes can be seen in Fig. 8a where we plot $(\overline{g'^2})^{1/2}$ normalized with respect to $B_0^{2/3}/H^{1/3}$, the nonrotating limit, as a function of depth. There is a systematic shift of the profiles with rotation, g' increasing with rotation rate. In Fig. 8b, however, we normalize $(\overline{g'^2})^{1/2}$ with respect to $\sqrt{B_0 f}$ and plot it against depth and in Fig. 8c against depth normalized with respect to l_{rot}. The collapse of the data from the high-rotation experiments is very reasonable and strongly supportive of the scaling given in Eq. (9). Note that again, and as expected, it is only the low-rotation experiments that fail to be normalized.

Of particular note is the vertical variation of $(\overline{g'^2})^{1/2}$ as revealed in Fig. 8b. In each of the profiles we can see the transition from the thermal boundary layer in the upper levels of the column, to the rotationally dominated layer beneath, in which all the curves (except $f = 10^{-6}$ s^{-1}) converge on the rotational scaling $\sqrt{B_0 f}$. At high rotation the thermal boundary layer is shallow and the rotational layer deep. At lower rotation rates the thermal boundary layer extends to deeper levels as one would expect if it is depth scaled with l_{rot}.

2) CONES

The combined effect of the many current solenoids on the plume scale is to drive an increasingly strong, large-scale rim current around the disk of cooling, cyclonic at the surface, anticyclonic beneath. This rim current serves to confine the convected fluid to the volume defined by the disk of cooling. Fluid outside the chimney is unmodified, and there is little lateral transfer of fluid between the overturning and the nonoverturning regions. By day 2, however, there is evidence of the growth of meanders in the rim current as it becomes baroclinically unstable, an instability that eventually leads to the breakup of the patch of convected water. In the first two days strong vertical motions associated with upright convection within the chimney retard the growth of baroclinic eddies and allow time for the buildup of potential energy. But after two days the cooling from the surface ceases and with it, convective activity; vertical velocities rapidly fall back to a fraction of their forced value, and there is a corresponding growth in the amplitude of the rim current instability as it extracts stored potential energy. Beyond two days baroclinic processes proceed unhindered. By day 4 (see Fig. 9) the chimney of homogenized cold water has broken up into a number of distinct conical structures extending throughout the depth of the model ocean. These cones have a definite space and velocity scale.

A clear view of the geometry of the cones is provided by Fig. 10 where a 3D isothermal surface is plotted at the end of day 4 for the reference experiment. The cones contain convectively modified water that is prevented from slumping to the ocean floor by the earth's rotation. The currents associated with the cones are surface intensified and cyclonic in sense, weaker, and anticyclonic at depth. We interpret the predominance of cyclonic vorticity as a consequence of the vigorous stretching of vortex tubes in the sinking motion resulting in a concentration of cyclonic vorticity in the convected fluid.

We estimate from Figs. 9 and 10 that in the reference experiment the aspect ratio of these cones of convected fluid, the end state of the convective process, is $l_{\mathrm{cone}}/H \sim 7.6$ km/2 km $= 3.8$, where l_{cone} is the diameter of the cone. According to the scaling ideas presented in section 3, this ratio should scale as $\sqrt{\mathrm{Ro}^*}$; indeed Fig. 9 vividly demonstrates that the horizontal scale of the cones decreases with increased rotation rate. The ratio l_{cone}/H is plotted in Fig. 11a, for points obtained from all the experiments set out in Table 3, as a function of $\sqrt{\mathrm{Ro}^*}$. We see that the points all fall onto a straight line. In Fig. 11b we plot the same points but now along with data obtained by Maxworthy and Narimousa (1993) in the laboratory. It is very pleasing to find that the laboratory and numerical experiments collapse on a very similar line; taken together they are strongly supportive of the cone scaling (12). From the slope of the line drawn through the data in Fig. 11 we deduce that

FIG. 7. The vertical velocity field at a depth of 1 km at day 2 revealing the horizontal scales associated with the plumes. (a) $f = 5 \times 10^{-4}$ s^{-1} ($w_{\mathrm{min}} = -9$ cm s^{-1}; $w_{\mathrm{max}} = 9$ cm s^{-1}), (b) $f = 3 \times 10^{-4}$ s^{-1} ($w_{\mathrm{min}} = -14$ cm s^{-1}; $w_{\mathrm{max}} = 9$ cm s^{-1}), (c) $f = 2 \times 10^{-4}$ s^{-1} ($w_{\mathrm{min}} = -13$ cm s^{-1}; $w_{\mathrm{max}} = 11$ cm s^{-1}), (d) $f = 1 \times 10^{-4}$ s^{-1} ($w_{\mathrm{min}} = -18$ cm s^{-1}; $w_{\mathrm{max}} = 9$ cm s^{-1}), (e) $f = 0.8 \times 10^{-4}$ s^{-1} ($w_{\mathrm{min}} = -19$ cm s^{-1}; $w_{\mathrm{max}} = 9$ cm s^{-1}), and (f) $f = 0.5 \times 10^{-4}$ s^{-1} ($w_{\mathrm{min}} = -21$ cm s^{-1}; $w_{\mathrm{max}} = 10$ cm s^{-1}). The dashed line is the zero contour.

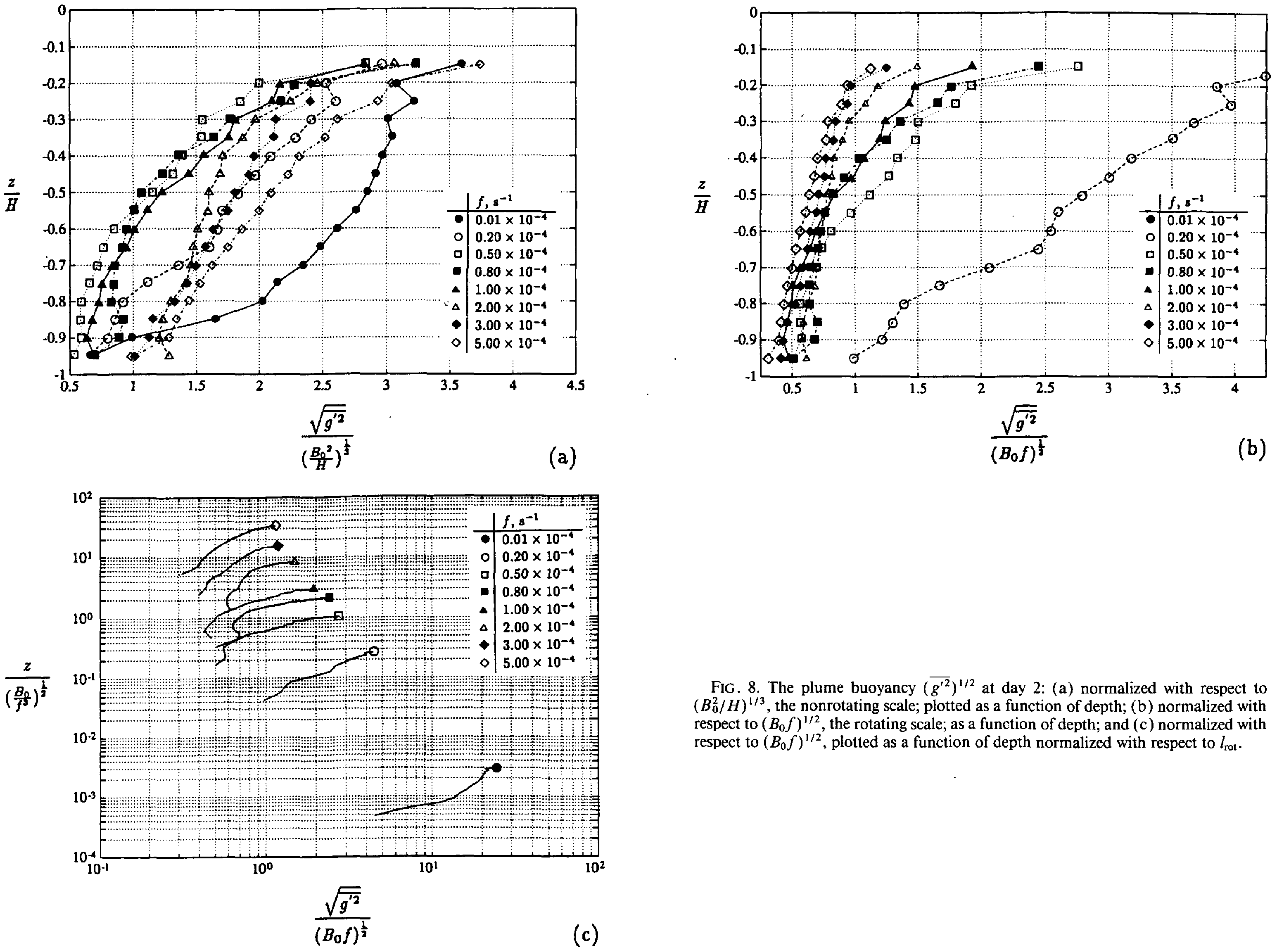

FIG. 8. The plume buoyancy $(\overline{g'^2})^{1/2}$ at day 2: (a) normalized with respect to $(B_0^2/H)^{1/3}$, the nonrotating scale; plotted as a function of depth; (b) normalized with respect to $(B_0 f)^{1/2}$, the rotating scale; as a function of depth; and (c) normalized with respect to $(B_0 f)^{1/2}$, plotted as a function of depth normalized with respect to l_{rot}.

$$\frac{l_{\rm cone}}{H} \sim 5 \times \sqrt{\rm Ro^*}. \qquad (31)$$

In Table 4 the velocity and space scale of the cones of adjusted fluid observed in our numerical experiments are set out; empirically we observe that there is an excellent correspondence between the natural Rossby number Ro* based on the external parameters in each experiment [Eq. (13)] and that deduced from our numerical data in Table 4. Physically one might argue that the plumes fill out vertically as well as horizontally, from $l_{\rm rot}$ to H, so that the Rossby number decreases from $1 = u_{\rm rot}/fl_{\rm rot}$ to $\mathrm{Ro}^* = u_{\rm rot}/fH$. Such reasoning is suggestive of the following velocity scaling for the cone.

Since we observe that

$$\mathrm{Ro}_{\rm cone} = \frac{u_{\rm cone}}{fl_{\rm cone}} \sim \mathrm{Ro}^*$$

and

$$l_{\rm cone} \sim l_\rho = H\sqrt{\rm Ro^*},$$

then it follows that

$$u_{\rm cone} \sim fH\,\mathrm{Ro}^{*\,3/2} = \frac{B_0^{3/4}}{H^{1/2}f^{5/4}}. \qquad (32)$$

From Table 4 we do indeed observe that the cone velocity in our experiments decreases markedly as the rotation rate is increased.

Equation (32) may be expressed equivalently thus:

$$\frac{u_{\rm cone}}{u_{\rm rot}} \sim \sqrt{\rm Ro^*}, \qquad (33)$$

where we have divided by $u_{\rm rot} = (B_0/f)^{1/2}$ [Eq. (8)]. In Fig. 12 we plot the horizontal cone velocity observed in our high-rotation experiments (normalized with respect to $u_{\rm rot}$) against $\sqrt{\rm Ro^*}$. The points fall onto a rising curve, albeit with some scatter, broadly in support of the scaling [Eq. (33)]. For completeness we also plot in Fig. 12 the normalized rms plume velocity (averaged over the depth of the ocean at day 2); it is weakly dependent on $\sqrt{\rm Ro^*}$ as suggested by (8).

b. Low rotation

The two lowest rotation simulations in this study ($f = 0.01 \times 10^{-4}$ s^{-1} and $f = 0.2 \times 10^{-4}$ s^{-1}) turn out to be in a markedly different dynamical regime from those carried out at higher values of f. This is clearly demonstrated by the failure of low rotation data to collapse according to the rotationally constrained scalings presented in section 3a(2) (see, e.g., Figs. 6b and 6c). Significantly better collapse is achieved, especially in the $f = 0.01 \times 10^{-4}$ s^{-1} (essentially nonrotating) case, by the depth-constrained, nonrotating scalings [Eq. (6); Fig. 6a].

While enhanced rotation tends to reduce the plume scale and inhibit deepening, at reduced rates of rotation such that $l_{\rm rot} \gg H$ the scale of the plumes, and thereby their depth of penetration, is limited by the vertical extent of the ocean in advance of significant rotational control. As the rotation rate is reduced, $u_{\rm plume}$ and $l_{\rm plume}$ grow in magnitude—the mixed chimney deepens as the cells, sweeping the cooled fluid out of the boundary layer, swell to fill the model ocean. If $l_{\rm rot}$ exceeds H, the plumes are constrained by the depth of the ocean and have a characteristic velocity smaller than the rotational scaling predicts. From Table 3 it can be seen that the rms horizontal velocity $(u'^2 + u'^2)^{1/2}$ midway down the model ocean (taken to be a measure of $u_{\rm plume}$) is significantly lower than $u_{\rm rot}$. For example, when $f = 0.01 \times 10^{-4}$ s^{-1}, $u_{\rm rot}$ has six times the value of the observed $u_{\rm plume}$. Instead, the appropriate velocity scaling is $(B_0H)^{1/3}$.

The transition to a new scaling regime under slowly rotating conditions is also reflected in the variation of $(\bar{g}'^2)^{1/2}$ a measure of the buoyancy associated with the plumes and the cones. Maxworthy and Narimousa (1993) suggest that if $\mathrm{Ro}^* \sim 1$ then $g'_{\rm norot}$ might be adopted as the cone buoyancy scale implying that $l_{\rm cone}/H \sim \sqrt{g'_{\rm norot}H}/f \sim (\mathrm{Ro}^*)^{2/3}$. The points plotted in Fig. 11b from our numerical model do indeed appear to fall on a curve that, as Ro* approaches unity, has a slope somewhat greater than the one implying an $\sqrt{\rm Ro^*}$ dependence.

The (very) low-rotation simulations are also *qualitatively* different from the high-rotation experiments. In slowly rotating conditions the thermally forced, surface convergence does not come under geostrophic control and is strongly radial; cold fluid is flushed out laterally at the base of the chimney reaching speeds of 30 cm s^{-1}. There is a reduction in the overall scale of the sinking region relative to that of the applied cooling, with the strongest descent occurring in a ring a few kilometers inside the cooling disk. Vertical velocities in this region exceed 20 cm s^{-1} downwards in the $f = 0.01 \times 10^{-4}$ s^{-1} case. Vertical mixing in the interior of the sinking region is characterized by a small number of rather "flabby," less energetic plumes, with cooled fluid being squeezed out to the sides of the chimney. The extreme vigor and large scale of the outflow in these low-rotation experiments, taken together with the very limited extent of our computational domain, meant that it was not possible to continue these simulations beyond 48 hours.

6. Theoretical interpretation

The foregoing experiments were interpreted by physically motivated scaling arguments without recourse to the results of detailed linear stability analysis. A number of theoretical issues, however, are raised by our study for which linear theory may be pertinent.

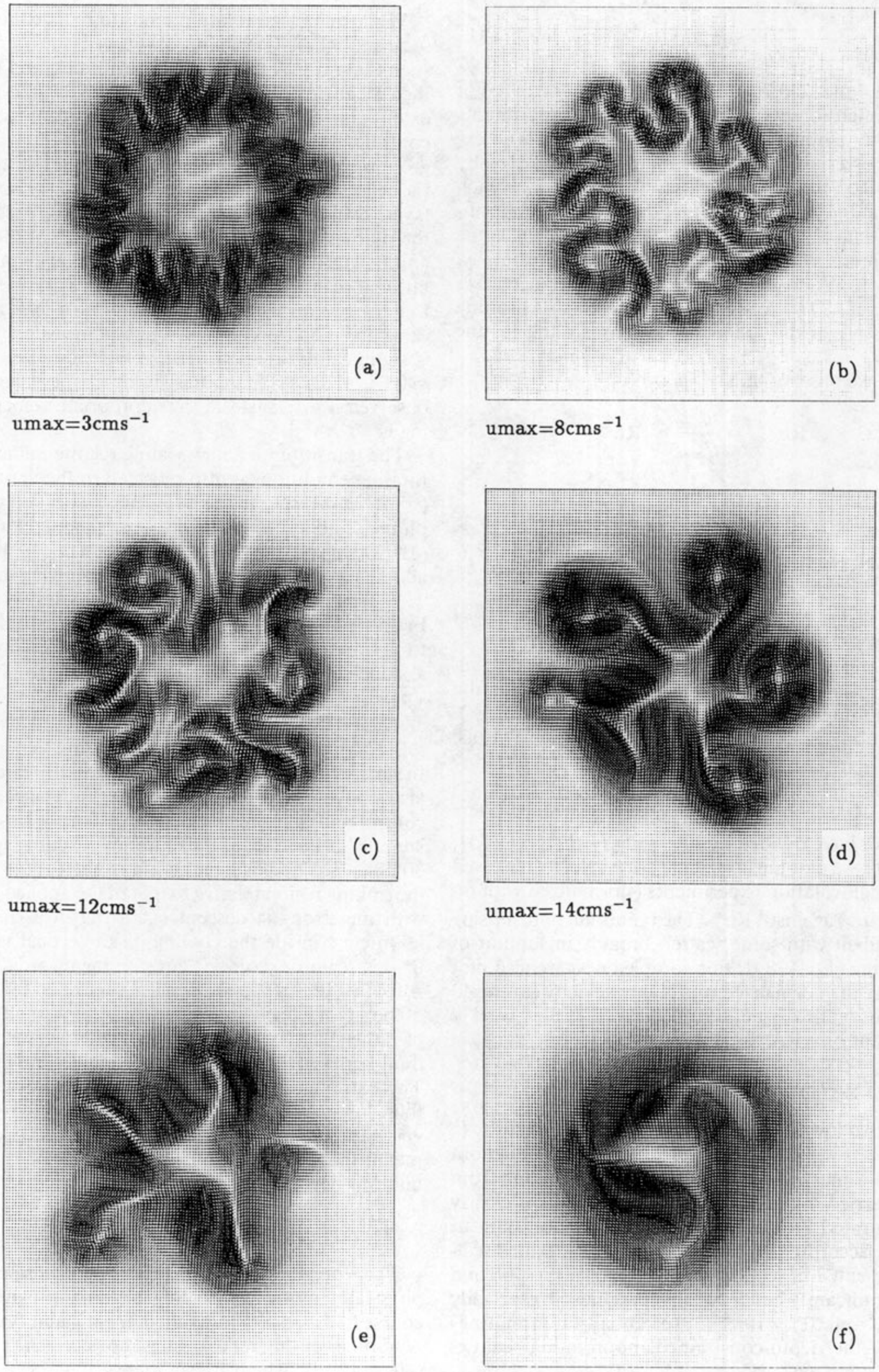

umax=3cms^{-1}

umax=8cms^{-1}

umax=12cms^{-1}

umax=14cms^{-1}

umax=17cms^{-1}

umax=21cms^{-1}

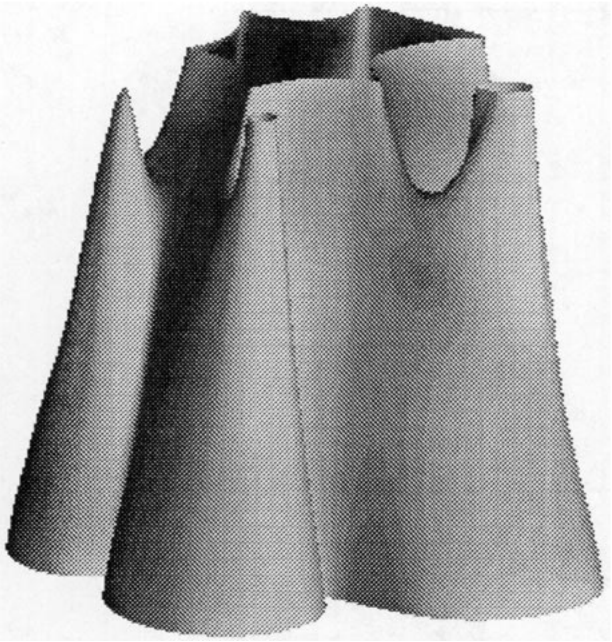

FIG. 10. The geometry of an isothermal surface illustrating the morphology of the cones in the reference experiment at the end of day 4.

Perhaps the most difficult and problematical is an understanding of those factors that control the initial scale of the plumes in the model. As described in section 6b, linear Rayleigh–Taylor instability theory has been employed to provide a guide to the preferred plume scale, interpreting the viscosity and thermal diffusivity as the eddy coefficients used in our numerical model. The horizontal scale of the plumes is indeed broadly consistent with that of the marginally unstable wave in the thermal boundary layer of depth h over which our forcing maintains a temperature inversion. First, however, we interpret the space and time scales of the cones of convected fluid observed in our experiments in terms of baroclinic instability theory. These scales are independent of the precise details of the plumes themselves.

a. Baroclinic instability theory

A key but robust element of the scaling arguments of section 3 is that the lateral dimension of the cones scales with the radius of deformation. There is very strong support for this observation from the theory of baroclinic instability developed by Eady (1949) and followers. The analysis most relevant to our present problem is that of Pedlosky (1985). He was motivated, in part, by the "exploding heton" cloud experiments of Hogg and Stommel (1985), which is the focus of a companion paper by Legg and Marshall (1993).

Pedlosky considered the instability of a baroclinic rim current generated by circular regions, radius r_0, of piecewise constant potential vorticity in a two-layer quasigeostrophic system, cyclonic in the upper layer and anticyclonic beneath. As in all stability analyses, the radius of deformation L_ρ is associated with an ambient, specified stratification and not with one that is internally generated, as here, by a convective process.

If $r_0 \gg L_\rho$ then Pedlosky's problem reduces to that considered by Eady (1949) and the vortex is unstable to perturbations of the boundary of mode number m provided that

$$m \leqslant \sqrt{2}\,\frac{r_0}{L_\rho}. \qquad (34)$$

Equation (34) is a statement of the requirement to "fit" waves around the perimeter of the large-scale vortex. Thus, a vortex with radius greater than $\sqrt{2}L_\rho$ will be unstable to infinitesimal perturbations. Furthermore, the wavelength of the fastest-growing mode scales with the radius of deformation. From (12) we expect m, the wavenumber of the instability observed on the rim current, to depend inversely on $\sqrt{\mathrm{Ro}^*}$. This is indeed observed in our experiments (see Fig. 13 which plots m^{-1} as deduced by inspection of plots such as Fig. 9, against $\sqrt{\mathrm{Ro}^*}$).

The Eady growth rate of the most unstable mode is

$$\omega_{\mathrm{Eady}} = mc_i = \frac{0.3f}{\sqrt{\mathrm{Ri}}}, \qquad (35)$$

where $\mathrm{Ri} = N^2/(dv/dz)^2$ is the Richardson number associated with the large-scale flow and c_i is the imaginary component of the phase speed. Here, we interpret N^2 and dv/dz as (constant) Brunt–Väisälä frequency and velocity shears associated with the rim current.

The Ri appropriate to the present study, formed from external parameters, is

$$\mathrm{Ri} = \frac{g'_{\mathrm{rot}}H}{u_{\mathrm{cone}}^2} = \frac{f^3H^2}{B_0} = \frac{1}{\mathrm{Ro}^{*2}},$$

where we have substituted for u_{cone} making use of Eq. (32) or

$$\mathrm{Ri}\,\mathrm{Ro}^{*2} = 1. \qquad (36)$$

It is pleasing to again see Ro* as the fundamental parameter of our problem and quasigeostrophic scaling

---

FIG. 9. The pattern of horizontal currents at a depth of 200 m after four earth days for (a) $f = 5 \times 10^{-4}\ \mathrm{s}^{-1}$ ($u_{\max} = 3\ \mathrm{cm\ s}^{-1}$), (b) $f = 3 \times 10^{-4}\ \mathrm{s}^{-1}$ ($u_{\max} = 8\ \mathrm{cm\ s}^{-1}$), (c) $f = 2 \times 10^{-4}\ \mathrm{s}^{-1}$ ($u_{\max} = 12\ \mathrm{cm\ s}^{-1}$), (d) $f = 1 \times 10^{-4}\ \mathrm{s}^{-1}$ ($u_{\max} = 14\ \mathrm{cm\ s}^{-1}$), (e) $f = 0.8 \times 10^{-4}\ \mathrm{s}^{-1}$ ($u_{\max} = 17\ \mathrm{cm\ s}^{-1}$), and (f) $f = 0.5 \times 10^{-4}\ \mathrm{s}^{-1}$; ($u_{\max} = 21\ \mathrm{cm\ s}^{-1}$).

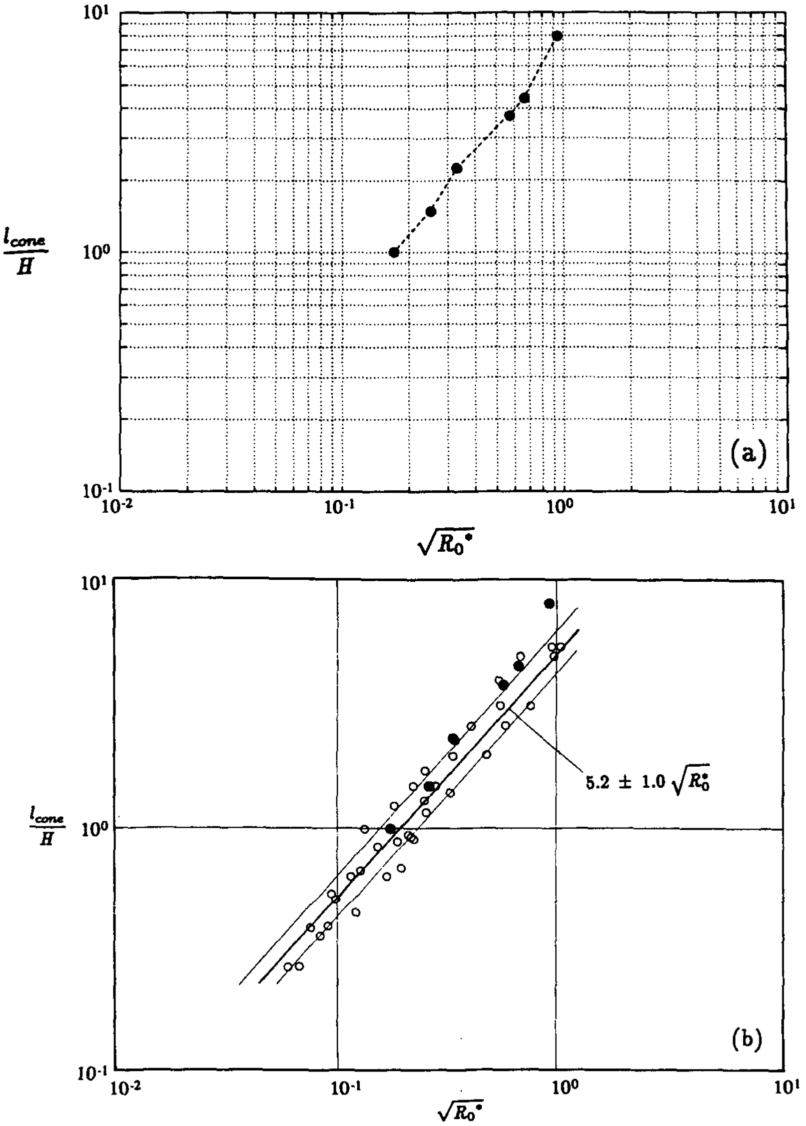

FIG. 11. (a) The aspect ratio of the cones, l_{cone}/H, plotted against Ro* for our six high-rotation experiments. (b) The aspect ratio of the cones, l_{cone}/H, plotted against Ro* for our six high-rotation numerical experiments superimposed on the data obtained by Maxworthy and Narimousa (1993) in their laboratory.

(36) emerging.[7] If Ro* is small then Ri will be large and the balanced motion quasigeostrophic; note that Ro* is also a measure of the Rossby number on the cone (geostrophic) scale.

Thus, from Eq. (35) the Eady growth rate scales as

$$\omega_{\text{Eady}} \sim f\text{Ro}^* = \frac{1}{H}\left(\frac{B}{f}\right)^{1/2} = \frac{u_{\text{rot}}}{H}. \qquad (37)$$

For a fixed magnitude of cooling B_0, the growth rate diminishes as f increases; the time scale of the baroclinic processes creating the cones increases with increasing rotation rate, both relative to the rotation period and in absolute terms. This deduction should be contrasted with that implied by quasigeostrophic theory [Eq. (35)] in which the reduced gravity (rather than the buoyancy flux) is specified and growth rates are faster at higher f. Inspection of Fig. 9, which presents flow fields after four earth days for a range of rotation periods, suggests that baroclinic instability has indeed reached finite amplitude, forming cutoff coherent cones, at lower rather than higher rotation rates, consistent with arguments leading to (37).

---

[7] In the Eady problem and quasigeostrophic theory, the Ri number is the controlled and controlling parameter. The Rossby number of the ensuing motion is such that Eq. (36) is satisfied and is small if Ri is large.

TABLE 4. Horizontal velocity and space scales of the cones observed at day 4 in the high-rotation experiments.

$f(\times 10^4)$ (s^{-1})	u_{cone} ($m\ s^{-1}$)	l_{cone} (km)	Ro_{cone}	Ro*
0.5	0.17	16.8	0.41	0.89
0.8	0.17	8.8	0.48	0.44
1.0	0.10	7.6	0.27	0.32
2.0	0.08	4.6	0.17	0.11
3.0	0.04	3.0	0.09	0.06
5.0	0.02	2.0	0.04	0.03

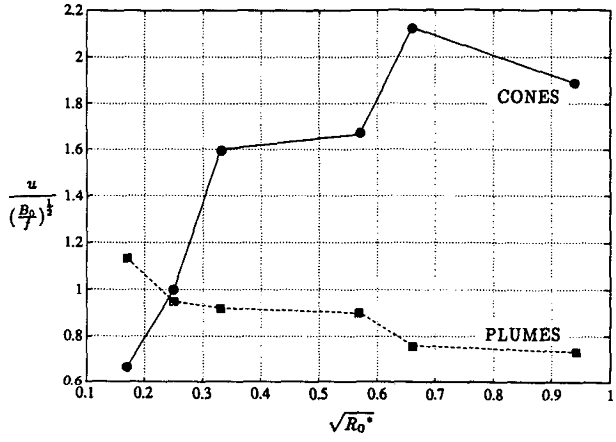

FIG. 12. Graphs of u_{cone} and u_{plume} normalized with respect to u_{rot}, plotted against Ro*.

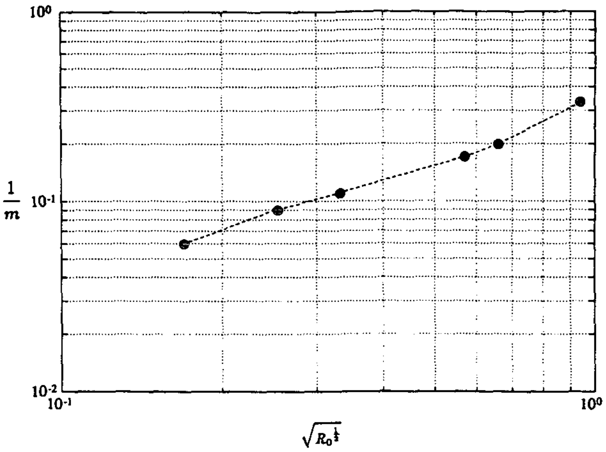

FIG. 13. A graph of $1/m$, where m is the wavenumber of the rim current instability observed in Fig. 9, plotted against Ro*.

b. Rayleigh theory

The horizontal scale of the plumes and their aspect ratio in the initial phases of the convective process is broadly consistent with linear theory if it is supposed that the unstable layer has a depth given by h, the vertical extent of the temperature inversion. The applied cooling induces a temperature inversion in the top two layers of the model; inspection of hydrographic sections at 6 hours reveals a temperature inversion of ~0.01 to 0.02 K in the surface 200 m. In a fluid devoid of viscosity any such inversion will be statically unstable and lead to the growth of convective cells that overturn the layer and, as they grow to finite amplitude, extend down into the neutral fluid beneath. As first demonstrated by Rayleigh (1916), however, in the presence of viscosity a critical temperature gradient must be exceeded before overturning is allowed. In our simulation the strength of the inversion grows in time until it exceeds some critical value, at which point it rapidly overturns by generating plumes which flux the cold fluid out of the surface boundary layer to depth. We now enquire into those factors that control the magnitude of the required inversion and the scale of the ensuing convection. The Taylor number, Ta, appropriate to our unstable thermal boundary layer,

$$\mathrm{Ta} = \frac{f^2 h^4}{(K^v)^2},$$

is about 400 (choosing $f = 10^{-4}\ s^{-1}$, $h = 200$ m, $K^v = 0.2\ m^2\ s^{-1}$) and sufficiently small that we shall be content to apply nonrotating Rayleigh theory to guide our interpretation of the early, linear phase of the plume's life (see Chandrasekhar 1961). Classical Rayleigh theory cannot, however, be applied directly to our simulation because our diffusion operator, Eq. (22), is anisotropic (K^h is not equal to K^v). In appendix B we consider marginally unstable infinitessimal perturbations to a resting fluid confined between two rigid, free boundaries a distance h apart in which the temperature decreases linearly with height and $K^h \gg K^v$. Two nondimensional parameters define the system,

$$r^2 = \frac{K^h}{K^v}$$

and

$$\mathrm{Ra} = \frac{g\epsilon h^4 \beta}{(K^v)^2},$$

a Rayleigh number based on the vertical eddy coefficient and $\beta = dT/dz$ the constant adverse temperature gradient, ϵ is the coefficient of expansion of water.

In all our numerical experiments $r^2 = 25$ and we find[8] (see appendix B) that the extreme value, the smallest possible for which steady motion exists, is

---

[8] Because r^2 is large our analysis is insensitive to the nature of the thermal condition (i.e., whether the temperature or its flux is specified) at the upper and lower boundary.

$$\mathrm{Ra}_c = 10\,146,$$

at which point a, a measure of the aspect ratio of the cells, takes on the value 0.64. The wavelength of the marginal wave is

$$\lambda = \frac{2\pi h}{a} \approx 9.8h \qquad (38)$$

and independent of K^v.

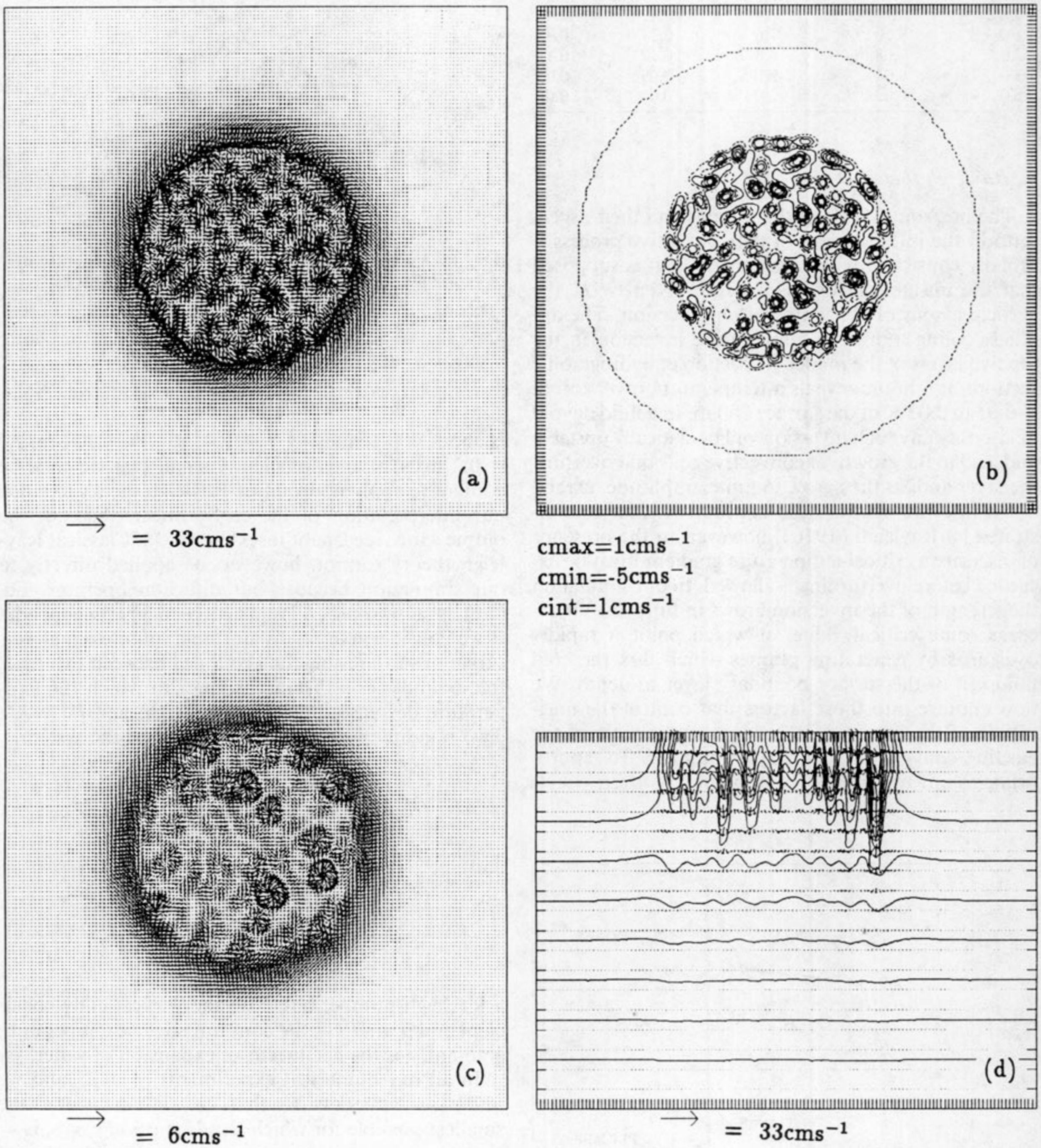

FIG. 14. The weakly stratified, chimney simulation at 12 hours. (a) The pattern of horizontal currents at 200 m over the 32 km square doubly periodic domain. Arrows are plotted at each grid point of the model. (b) The pattern of vertical velocity over the domain at a depth of 500 m. The contour interval is 1 cm s^{-1}. The dashed line is the zero contour. The ticks, every 250 m, indicate the horizontal resolution of the model. (c) The pattern of horizontal currents at 1 km. (d) An east–west section through the middle of the developing chimney showing temperature contours and the velocity field in the plane of the section. The ticks indicate the horizontal (250 m) and vertical (100 m) resolution of the model. The top-to-bottom temperature difference is 0.05 K.

In the preliminary stages of our experiment it seems reasonable to choose h, the vertical extent of the thermal boundary layer, to be the depth over which cooling is applied by the forcing function $\mathcal{F}$ in Eq. (29). Inserting numbers appropriate to our model simulation we find that ΔT, the temperature drop across the inversion, must exceed 0.025 K for the fluid to overturn. This is probably an overestimate since the effective h of the fluid is almost certainly greater than 200 m because, rather than a rigid boundary beneath the boundary layer, there is a neutral ocean beneath. Inspection of model fields from the reference simulation suggests that $(\overline{T'^2})^{1/2}$ at the base of the thermal boundary layer of the model is indeed $\sim$.025 K. At the rate of cooling applied to the model, an inversion of this magnitude can be created in only $\sim$6 hours.

The scale of the marginally stable wave as given by Eq. (38) (1900 m) is somewhat larger than the scale of the plumes seen in our simulation (see Table 3). As is clearly revealed in the simulations, however, nonlinearity cannot be neglected; indeed it dominates the evolution of the flow. Nevertheless the linear theory is suggestive of a scale selection process operating in the model, in the early part of a plume's life.

If it is supposed that in the ocean h is the depth to which the thermal boundary layer diffuses in a time f^{-1}—this distance is $(k/f)^{1/2}$, where k is the thermal diffusivity that characterizes the boundary layer—then Eq. (38) gives a plume scale of $\sim 9.8(k/f)^{1/2}$. If the vertical eddy diffusivity is ~ 1 m^2 s^{-1} in the near-surface layers during a period of strong buoyancy forcing—a value not inconsistent with the observations of Leaman and Schott (1991)—the corresponding scale of the marginally unstable mode is $\sim$900 m, roughly consistent with their inferences about the plume scale. It should, however, be emphasized that our predictions about the scale of the cones are not dependent on these details or assumptions.

7. Convection in a weakly stratified ocean

The foregoing experiments and scaling considered the convective overturning of a neutral ocean cooled at its upper surface. It is of interest to consider to what extent these ideas can be applied to the overturning of a weakly stratified ocean. One might expect that if $N \leqslant f$ then our scaling ideas will still provide a useful guide. To investigate we have carried out one extended integration simulating convection in a weakly stratified ocean; of the experiments presented, it is perhaps the most realistic and relevant to the observations of open-ocean convection collected by, for example, Schott and Leaman (1991), and is therefore described in some detail.

All parameters are identical to the reference experiment of section 5 except that now we set up a linearly stratified ocean with a top-to-bottom temperature difference of 0.05 K corresponding to an N^2 of 5×10^{-8} s^{-2} and a radius of deformation $L_\rho = NH/\pi f$ of 1.8 km. Critical parameters of our reference experiment are $l_{\mathrm{rot}} = 630$ m, $l_\rho = 1.1$ km (see Table 2) and so there is a "match" between the radius of deformation imposed externally by the stratification and that which will be internally generated by the convective process.

Figure 14 shows the velocity fields from the simulation at 12 hours and gives a vivid impression of the horizontal scales involved in the sinking process. The convection site is peppered with plumes; horizontal currents with speeds of $\sim$10 cm s^{-1} spiral around localized regions of sinking, cyclonically near the surface, anticyclonically at a depth of 1 km. The vertical velocity at 500 m suggests that there are some 50 individual elements each with a diameter of about 1 km. In the interior of the overturning region competition for fluid between adjacent plumes demands that some fluid be drawn in from outside, driving, by conservation of angular momentum, a large-scale circulation. Indeed, even at this early stage, one can see evidence of the development of a rim current around the perimeter of the convecting region. This is particularly evident in the magnified plot of the horizontal currents at 200 m shown in Fig. 15, which reveals the structure of the plumes and developing rim current in more detail.

The hydrographic section, Fig. 14d, taken along a horizontal line through the middle of the convection patch, shows plumes of dense fluid sinking down into

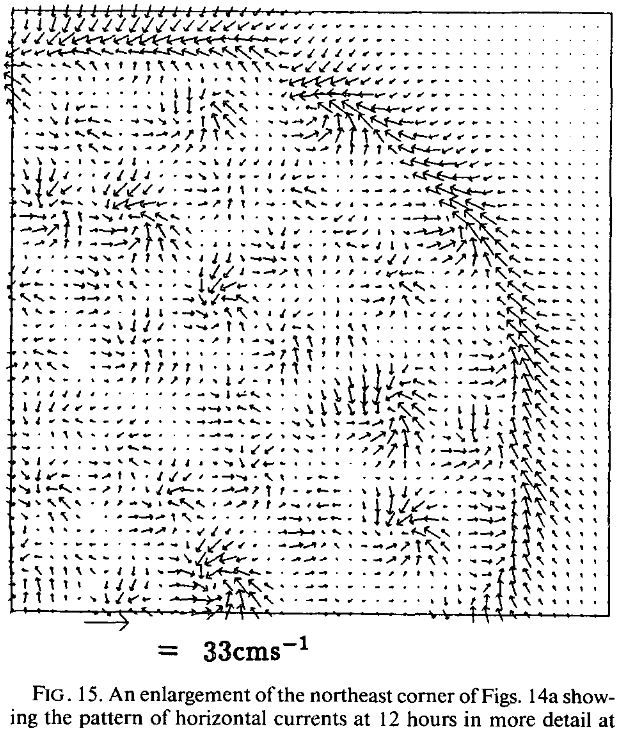

FIG. 15. An enlargement of the northeast corner of Figs. 14a showing the pattern of horizontal currents at 12 hours in more detail at a depths of 200 m.

the stably stratified fluid beneath with speeds of 10 cm s^{-1}. Undulations in the isopycnals at a depth of 1 km can be seen as dense fluid sinks. At the edge of the cooling region isopycnals rise sharply to the surface creating a baroclinic zone associated with the developing rim current.

By 24 hours (Fig. 16) a distinct rim current can be seen, cyclonic at the surface, anticyclonic beneath. Currents at 200 m are typically 10 cm s^{-1}, reaching 4–5 cm s^{-1} at depth. The horizontal scale of the plumes has expanded somewhat, as has the depth to which they penetrate. There is now evidence of an organized current system developing on the scale of the radius of deformation. Indeed by this time a marked correspondence between the pressure field (not shown) and the pattern of horizontal currents exists, in accord with the

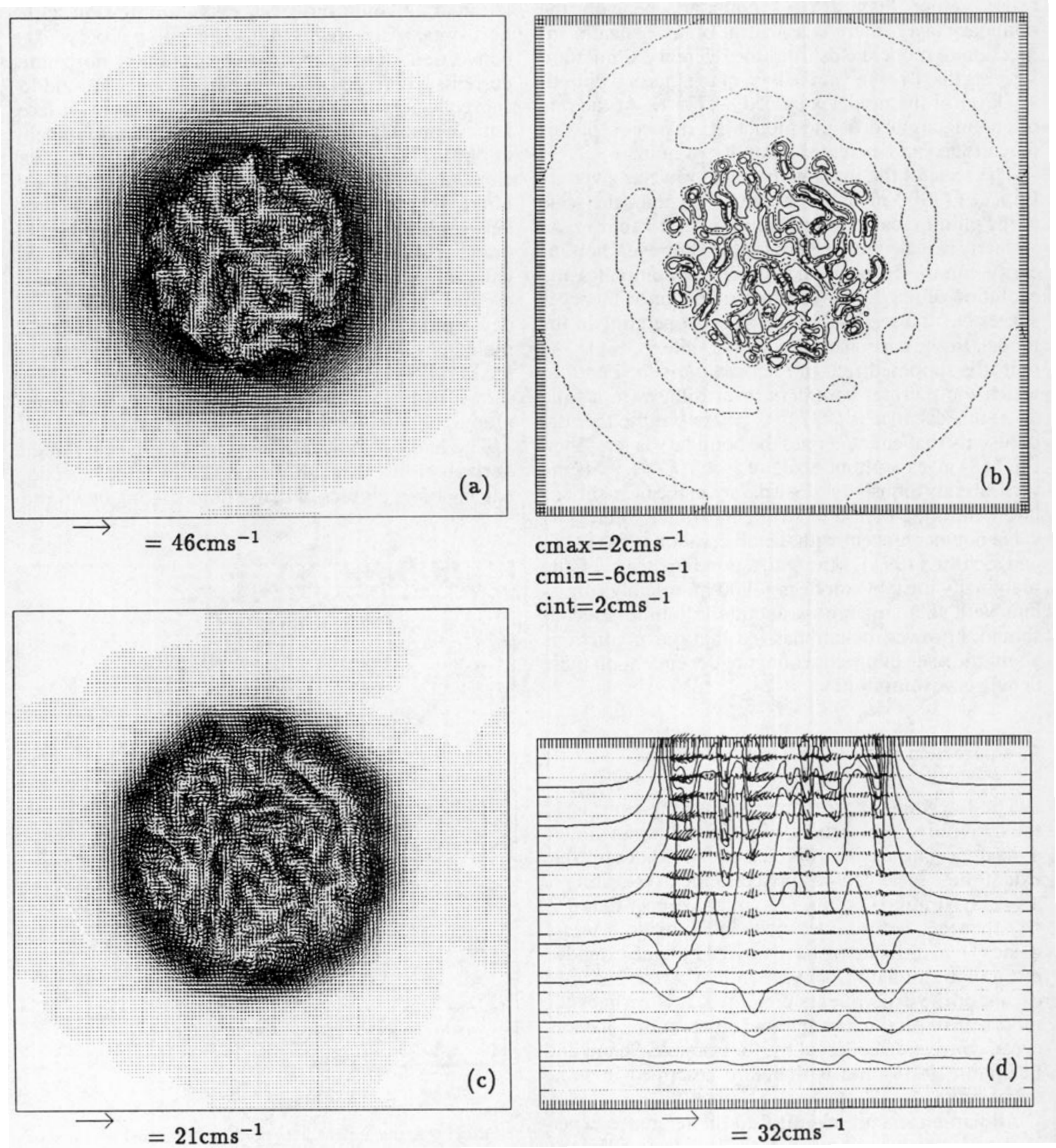

FIG. 16. The weakly stratified chimney simulation at day 1. The format is identical to Fig. 14.

geostrophic relation. The rim current is in thermal-wind balance with the sloping isopycnals at the edge of overturning region. The field of vertical velocity at 500 m has, as in the reference experiment of section 5, become organized into rolls suggestive of a control on the convective motion by the large-scale flow.

The hydrographic section at 24 h (Fig. 16d) reveals that the plumes now extend down to 1 km; vertical currents are ~10 cm s^{-1}, roughly in agreement with the $u_{\rm rot}$ scaling—a fluid particle at the surface only takes two or three hours to sink to 1 km. The w field shows a vertical coherence over the whole depth of the plume. Properties in the chimney are being efficiently mixed by plumes; water made dense at the surface plummets

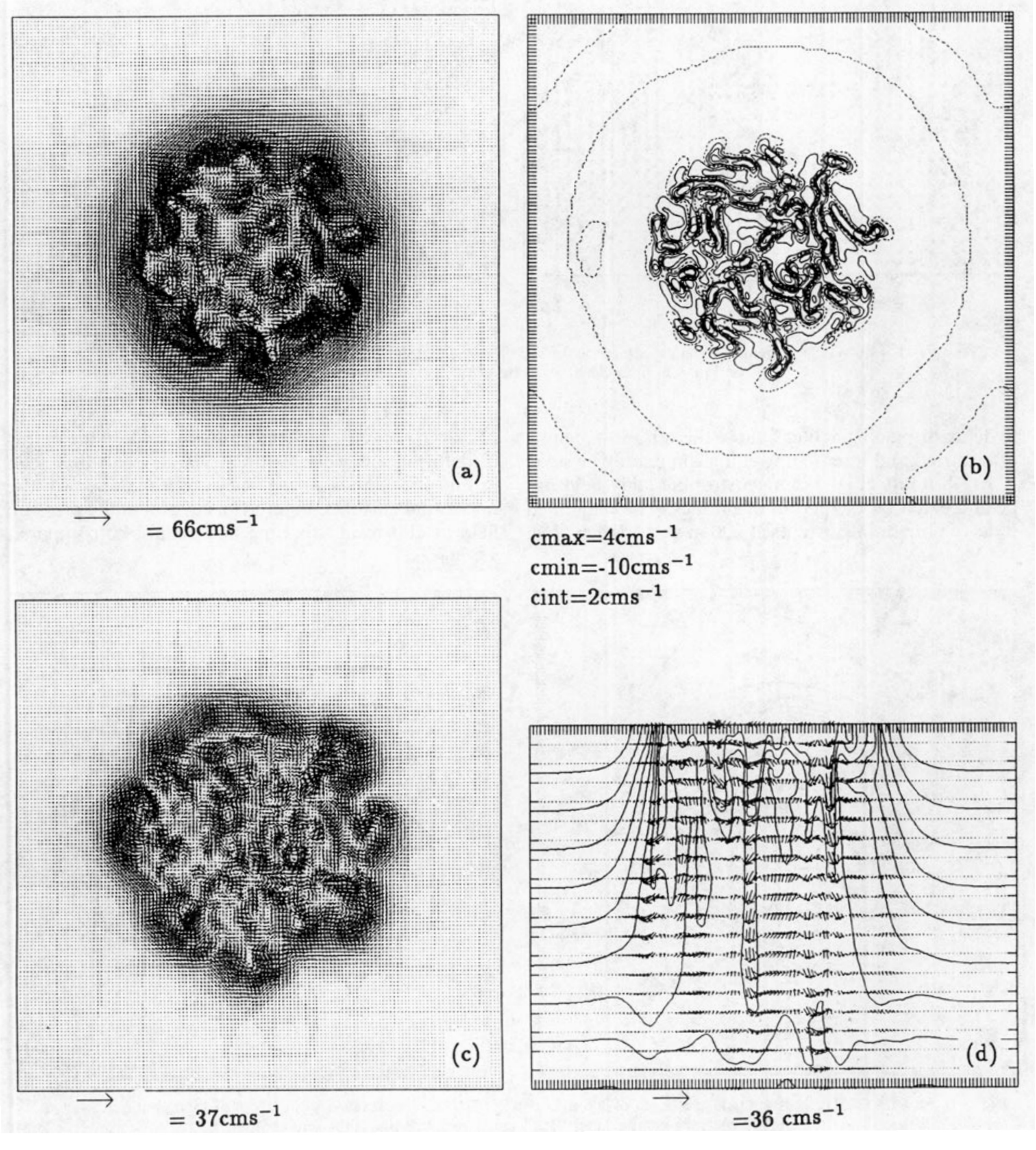

FIG. 17. The weakly stratified chimney simulation at day 2. The format is identical to Fig. 14.

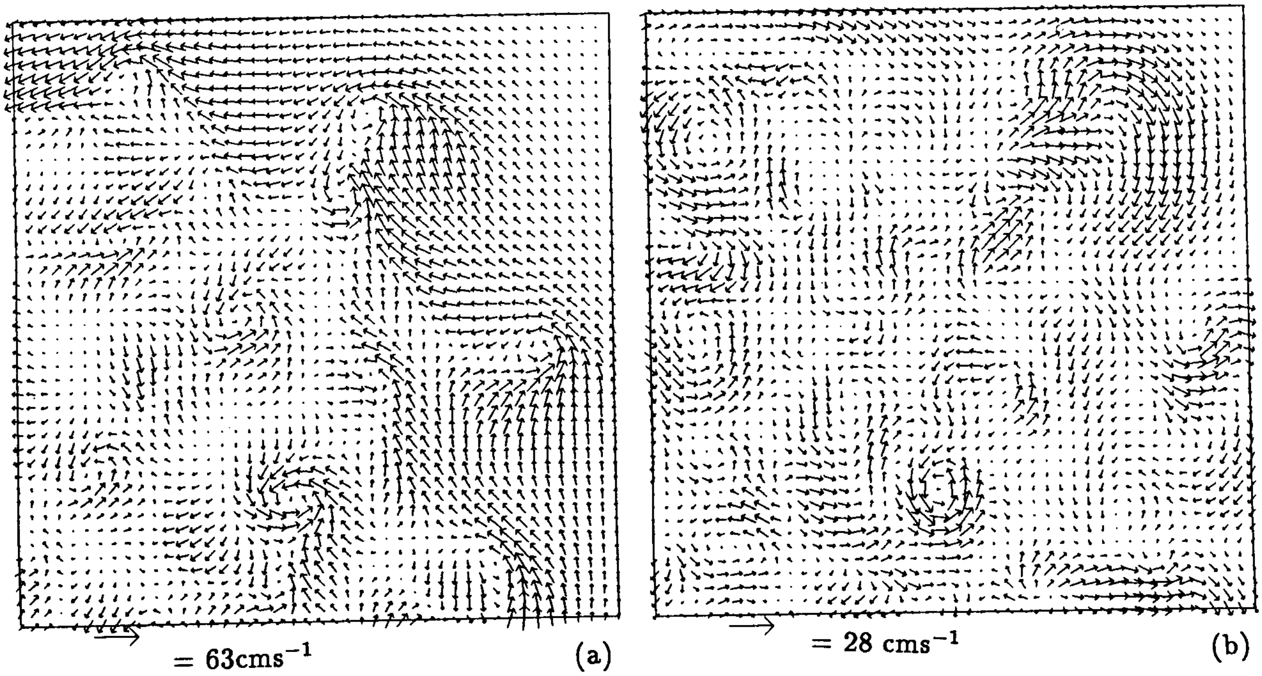

FIG. 18. An enlargement of the northeast corner of Figs. 17a and 17c showing the pattern of horizontal currents at 2 days in more detail at depths of (a) 200 m and (b) 1 km.

to depth displacing lighter fluid to the surface—regions of localized and intense upwelling can readily be seen.

At 48 hours (Fig. 17) a geostrophic eddy field has been created by the action of plumes. The magnified plots of horizontal currents at 200 m and 1000 m (Fig. 18) clearly reveal an intense eddying field on the radius of deformation scale, distinctly larger than that seen in Fig. 15; there is strong vertical shear present in the horizontal currents. Figure 19a is a plot of the pressure field at 200 m at this time and should be compared

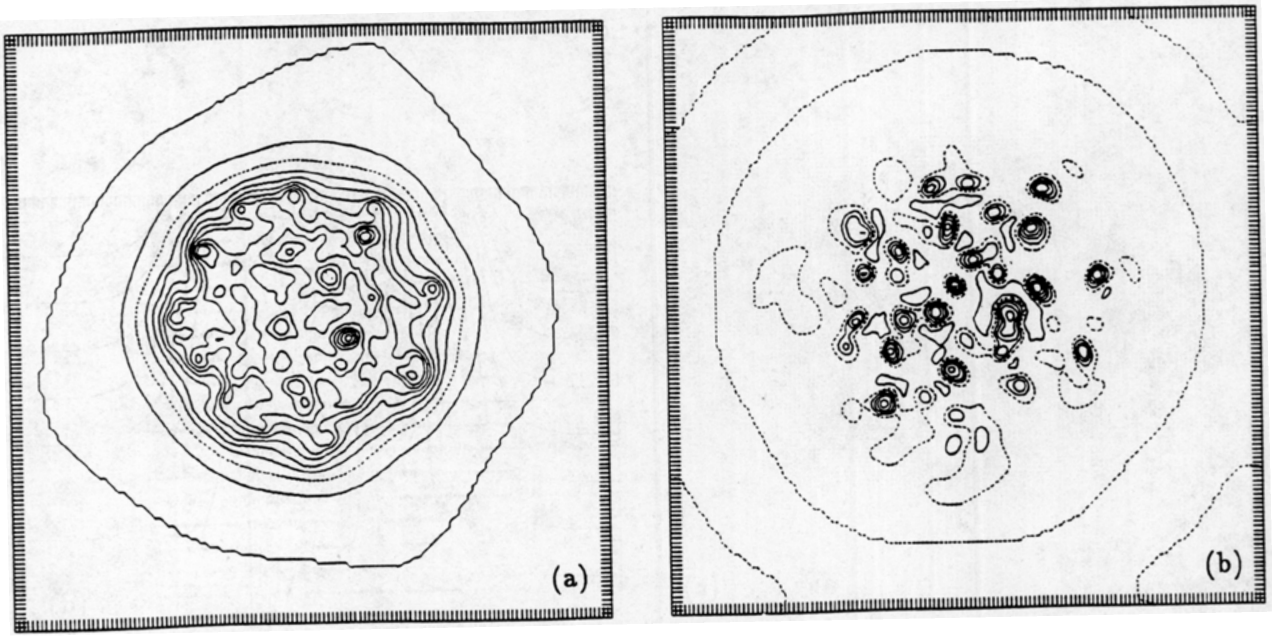

FIG. 19. (a) The pressure field at a depth of 200 m at day 2. (b) The vertical velocity at a depth of 1500 m at day 2. In both plots the contour interval is 1 cm. The dotted line is the zero contour.

with the pattern of currents in Fig. 17a. Evidently there is now strong geostrophic control on the motion with the mass and current field in balance; we estimate the plume Rossby number to be about 0.3. Furthermore, there is evidence of (~ mode 8) baroclinic instability of the rim current, as meanders begin to grow in the strong baroclinic zone at the periphery of the mixed region; however, coexisting with the geostrophic scale there are spectacular, almost vertical plumes pouring dense water down to the bottom (see Fig. 17d). Equally evident are coherent, strong upwelling regions compensating for the sinking. The vertical velocity at 1500 m at 48 hours (Fig. 19b) reveals the spatial pattern of plumes. Not all of the plumes have reached this

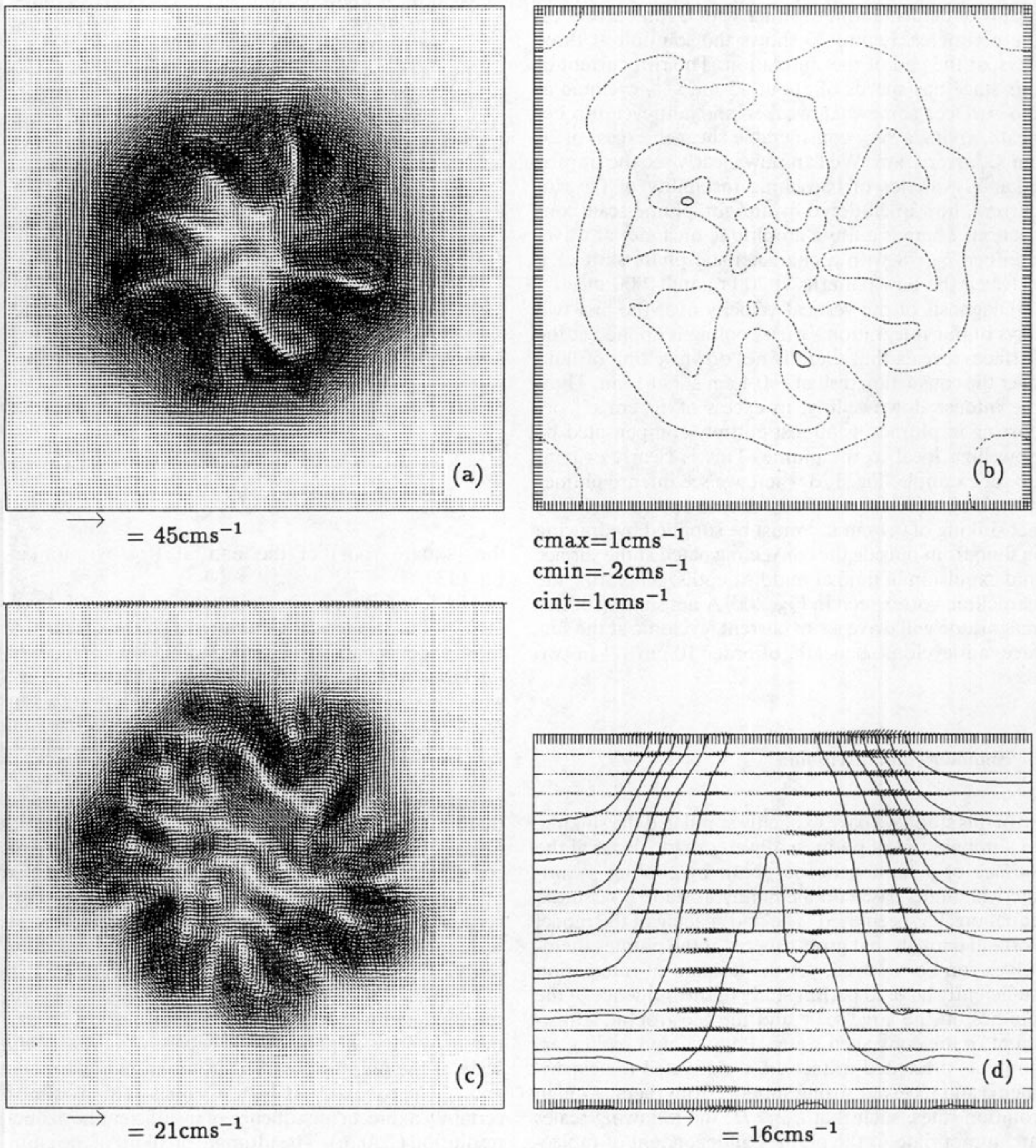

FIG. 20. The weakly stratified chimney simulation at day 3 with a format as in Fig. 14.

depth at this time but we estimate that there are about 30 active plumes with downwelling currents of about 10 cm s^{-1} penetrating to a depth of at least 1500 m.

At this point the cooling at the surface was switched off and the integration continued for a further day. On the cessation of cooling, overturning rapidly ceases; within 12 hours the vertical currents decay to about 1 cm s^{-1} in magnitude, leaving a quasi-horizontal geostrophic eddy field varying on the scale of the Rossby radius of deformation, together with a rim current on the perimeter. Figure 20 shows the solution at three days, at the end of the simulation. The rim current at this stage has speeds of about 15 cm s^{-1}, cyclonic at the surface, somewhat weaker and anticyclonic beneath, giving a very considerable shear in excess of 20 cm s^{-1} over 1 km. We can now clearly see the unmistakable evidence of baroclinic instability of the rim current, now uncluttered by upright, plume-scale convection. There is a finite-amplitude meander at wavenumber 7 or 8 with a characteristic phase shift of π between the flow patterns at 200 m and 1000 m.

Diagnosis of the vertical velocity over the first two days of our integration, when cooling is applied at the surface, reveals that there is net downwelling of fluid over the convection disk of ~0.1 cm s^{-1} at 1 km. Thus, the intense downwelling, in excess of 10 cm s^{-1} occurring in plumes, is almost entirely compensated by upwelling local to the plume. This is clearly evident in, for example, Fig. 17d where we see intense plumes of sinking and rising fluid adjacent to one another. The net sinking of 0.1 cm s^{-1} must be supplied by drawing in fluid from outside the convecting patch at the surface and expulsion of fluid at middle depths, generating the baroclinic vortex seen in Fig. 20d. A net sinking of this magnitude will drive a rim current, cyclonic at the surface, anticyclonic beneath, of order 10 cm s^{-1} in two days.

8. Summary and discussion

In this study we have explicitly simulated the sinking, in a population of plumes, of water made dense at the surface of a homogeneous ocean by cooling. A numerical model based on the nonhydrostatic Boussinesq equations has been used. The grid spacing of the model is small enough that gross aspects of the plumes themselves can be resolved, yet the domain of integration sufficiently large to permit study of the influence of the plumes on the large scale and the geostrophic adjustment of the convected water. Physical and scaling arguments presented in section 3 motivated the experiments and received strong support from them. At high rotation rates, such that $l_{\text{rot}} \leqslant H$, the following scales are appropriate to the plumes, independent of molecular and eddy viscosities and thermal diffusivities

$$l \sim l_{\text{rot}} = \left(\frac{B_0}{f^3}\right)^{1/2},$$

$$g' \sim g'_{\text{rot}} = (B_0 f)^{1/2},$$

$$u \sim u_{\text{rot}} = \left(\frac{B_0}{f}\right)^{1/2}.$$

Through the action of such rotationally controlled convection, a body of homogenized water—a chimney—is ultimately formed over the whole depth of the ocean. If, furthermore, rotation continues to inhibit mixing of overturned and ambient fluid, then the chimney will be characterized by the same buoyancy excess as that of the plumes that created it, g'_{rot}, and hence by a radius of deformation

$$l_\rho \sim \frac{\sqrt{g'_{\text{rot}} H}}{f}.$$

If, now, the chimney has a lateral scale larger than l_ρ, it must, through the mechanism of baroclinic instability, break up into fragments—cones—whose dimensions, invoking the theory of baroclinic instability, scale with its radius of deformation. Thus

$$l_{\text{cone}} \sim l_\rho,$$

or

$$\frac{l_{\text{cone}}}{H} \sim \sqrt{\text{Ro}^*},$$

the (square root) of the natural Rossby number, Eq. (13).

The foregoing physical picture has been substantiated by our numerical experiments to the extent that those experiments support the scaling laws derived on the basis of it. In particular, central to these ideas is a weak-mixing hypothesis that invokes rotation to suppress 3D turbulent motions. That the preceding cone scaling is borne out by Maxworthy and Narimousa (1993) in the laboratory and here by numerical experiment lends strong support to the physical ideas that lie behind it. It is particularly satisfying and significant that the numerical and laboratory experiments corroborate one another. That they do so indicates that our numerical experiments are not controlled by (uncertain) modeling assumptions concerning subgrid-scale processes and levels of eddy viscosity and diffusivity.

Finally, a number of important issues remain outstanding and will be the focus of future study. In particular there is a poor match between the *horizontal* scale of the plumes observed in the numerical model and l_{rot}, particularly at high f values. This is almost certainly a direct consequence of insufficient horizontal resolution (250 m). The ultimate breakup of the chimney of baroclinic eddies is only partially modeled here but is the focus of attention of the companion paper, Legg and Marshall (1992), where a heton model is used to represent the effect of geostrophically adjusted plumes on the large scale.

Acknowledgments. This study owes a great deal to Roger Brugge of Imperial College, who helped develop the computer programs that made it possible. Support was provided by grants from the MAST programme of the European Economic Community and the NOAA Climate Change Program. During the course of the work, advice from B. Cushman-Roisin, H. Fernando, J. Green, T. Maxworthy, D. Quadfasel, B. Rudels, F. Schott, U. Send, K. Speer, M. Stern, and J. Whitehead was of particular help.

APPENDIX A

The Hydrostatic Approximation

If, in standard notation,

$$\frac{Dw}{Dt} + g + \frac{1}{\rho}\frac{\partial p}{\partial z} = 0 \tag{A1}$$

is the vertical momentum equation with the height z as the vertical coordinate and $w = Dz/Dt$, then in the hydrostatic approximation the term Dw/Dt is omitted. But the condition for the validity of the hydrostatic approximation is much more stringent than $Dw/Dt \ll g$, the acceleration due to gravity, because almost all of g is balanced by the inert hydrostatic pressure gradient associated with the resting reference state.

More helpfully, we can isolate this hydrostatically balanced and dynamically inactive pressure gradient by writing the Boussinesq form of Eq. (A1) as

$$\frac{Dw}{Dt} + g\frac{\rho'}{\rho_0} + \frac{1}{\rho_0}\frac{\partial p'}{\partial z} = 0, \tag{A2}$$

where the primes denote a deviation from the hydrostatically balanced reference state and ρ_0 is a standard (constant) value of density. Now it can be clearly seen that the condition for the neglect of Dw/Dt is that it should be much smaller than $g' = g(\rho'/\rho_0)$ rather than g. Let us now try and estimate typical scales for which the hydrostatic approximation is valid, according to this more stringent condition.

Consider a convective event (in an unstratified ocean) which has a characteristic horizontal scale l and vertical scale H with horizontal and vertical velocity scales u and w, respectively. The time scale of a particle of fluid moving through the convective system is of order l/u and a typical w will be

$$w \sim \frac{uH}{l}.$$

So

$$\frac{Dw}{Dt} \sim \frac{u^2H}{l^2}$$

and hence $Dw/Dt \ll g'$ if[9]

$$\frac{u^2H}{g'l^2} \ll 1. \tag{A3}$$

If the condition (A3) is not satisfied then the full vertical momentum equation (A2) must be used.

a. Rotation not important

If rotation effects are not important then balancing inertial ($\sim u^2/l$) and horizontal pressure gradient ($\sim g'H/l$) terms in the momentum equation implies that $u^2 \sim g'H$, and the criterion (A3) becomes

$$\frac{H^2}{l^2} \ll 1,$$

the classical and familiar criterion.

b. Rotation important

If rotation effects are important then the balancing Coriolis and horizontal pressure gradient terms implies $u \sim g'H/fl$, and (A3) becomes

$$H^2 \ll \frac{l^4}{l_\rho^2}$$

where $l_p = \sqrt{g'H}/f$ or

$$\frac{H^2}{l_\rho^2} \ll 1 \quad \text{if} \quad l \sim l_\rho.$$

APPENDIX B

Rayleigh Theory with Anisotropic Diffusion

The marginally unstable wave satisfies steady forms of Eqs. (15)–(20), linearized about a state of rest; they can be written, neglecting rotation,

$$\nabla\left(\frac{p'}{\rho_0}\right) - g\epsilon\mathbf{k}T' = K^v\nabla_m^2\mathbf{v}',$$

$$w'\beta = K^v\nabla_m^2 T',$$

$$\nabla\mathbf{v}', \tag{B1}$$

where β ($= dT/dz$) is a constant lapse rate and

$$\nabla_m^2 = r^2\nabla_h^2 + \frac{\partial^2}{\partial z^2} \tag{B2}$$

---

[9] If the ambient fluid were stratified with Brunt–Väisälä frequency N^2, then the condition (A3) becomes $u^2/N^2l^2 \ll 1$.

is a modified Laplacian operator. Here,

$$r^2 = \frac{K^h}{K^v}, \qquad \text{(B3)}$$

the ratio of horizontal to vertical eddy coefficients, can be thought of as rescaling our horizontal coordinate. Note that if $r^2 = 1$ our problem reverts, with appropriate choice of boundary conditions, to the classical Rayleigh problem. Two nondimensional parameters define the system; taking the curl of the momentum equation and eliminating T', using the thermodynamic equation, leads to the following nondimensional equation containing only r^2 and a Rayleigh number[10]:

$$h^6\nabla^2\nabla_m^4 w' + h^2 \,\mathrm{Ra}\nabla_h^2 w' = 0, \qquad \text{(B4)}$$

where

$$\mathrm{Ra} = \frac{g\epsilon h^4\beta}{(K^v)^2} \qquad \text{(B5)}$$

is a Rayleigh number based on the vertical eddy coefficient.

If w' and w'_{zz} vanish at $z = 0, -h$, appropriate to rigid, free boundaries, Eq. (B4) has solutions of the form

$$w' \propto \sin\frac{\pi z}{h}\cos\frac{ax}{h},$$

provided that

$$(a^2 + \pi^2)(r^2a^2 + \pi^2)^2 = a^2\,\mathrm{Ra}. \qquad \text{(B6)}$$

Here a is a measure of the horizontal, compared to the vertical scale of the motion. The Rayleigh criterion is found from the condition that a be real. If $r^2 = 1$, then the cubic Eq. (B6) has real roots if

$$\mathrm{Ra} \geqslant \mathrm{Ra}_c = \frac{27\pi^4}{4} = 656.$$

In our simulation however, $r^2 = 25$, and we find that the extreme value, the smallest possible for which steady motion exists, is increased to

$$\mathrm{Ra}_c = 10\,146$$

at which $a = 0.64$, implying a wavelength for the marginal wave of

$$\lambda = \frac{2\pi h}{a} \approx 9.8h \qquad \text{(B7)}$$

independent of K^v. Thus, the scale of the marginally unstable wave is controlled by our choice of h, the depth assumed for the thermal boundary layer.

REFERENCES

Boubnov, B. M., and G. S. Golitsyn, 1990: Temperature and velocity field regimes of convective motions in a rotating plane fluid layer. *J. Fluid. Mech.*, **219**, 215–239.

Brugge, R., and J. C. Marshall, 1991: A non-hydrostatic ocean circulation model. Imperial College Int. Rep., 91 pp.

——, H. L. Jones, and J. C. Marshall, 1991: Non-hydrostatic ocean modelling for studies of open-ocean deep convection. *Proc. Workshop on Deep Convection and Deep Water Formation in the Oceans,* Monterey, Elsevier Science, 325–340.

Chandrasekhar, S., 1961: *Hydrodynamic Stability,* Dover.

Crépon, M., M. Boukthir, B. Barnier, and F. Aikman, 1989: Horizontal ocean circulation forced by deep-water formation. Part I: An analytical study. *J. Phys. Oceanogr.*, **19**, 1781–1793.

Deardorff, J. F., 1980: Stratocumulus-capped mixed-layers derived from a three-dimensional model. *Bound.-Layer Meteor.*, **18**, 495–527.

Eady, E. T., 1949: Long waves and cyclone waves. *Tellus,* **1**, 33–52.

Fernando, H. J. S., Boyer, D. L., and R. Chen, 1989: Turbulent thermal convection in rotating stratified fluids. *Dyn. Atmos. Oceans,* **13**, 95–121.

——, Rui-Rong Chen, and D. L. Boyer, 1991: Effects of rotation on convective turbulence. *J. Fluid Mech.*, **228**, 513–547.

Gascard, J.-C., 1978: Mediterranean deep water formation, baroclinic instability and oceanic eddies. *Oceanol. Acta,* **1**, 315–330.

Hogg, N., and H. Stommel, 1985: Hetonic explosions: The breakup and spread of warm pools as explained by baroclinic point vortices. *J. Atmos. Sci.*, **42**, 1465–1476.

Howard, L. N., 1964: Convection at high Rayleigh number. *Proc. 11th Int. Cong. Applied Mechanics,* 405–432.

Killworth, P. D., 1976: The mixing and spreading phases of MEDOC 1. *Progress in Oceanography,* Vol. 7, Pergamon, 59–90.

Leaman, K. D., and F. Schott, 1991: Hydrographic structure of the convection regime in the Gulf of Lions: Winter 1987. *J. Phys. Oceanogr.*, **21**, 573–596.

Legg, S., and J. Marshall, 1993: A heton model of the spreading phase of open-ocean deep convection. *J. Phys. Oceanogr.*, **23**, 1040–1056.

Madec, G., M. Chartier, P. DeLecluse, and M. Crépon, 1991: A three-dimensional numerical study of deep-water formation in the northwestern Mediterranean Sea. *J. Phys. Oceanogr.*, **21**, 1349–1371.

Maxworthy, T., and S. Narimousa, 1993: Unsteady deep convection in a homogeneous rotating fluid. *J. Phys. Oceanogr.*, submitted.

MEDOC Group, 1970: Observations of formation of deep water in the Mediterranean Sea, 1969. *Nature,* **227**, 1037–1040.

Miller, M. J., 1974: On the use of pressure as a vertical co-ordinate in modelling convection. *Quart. J. Roy. Meteor. Soc.*, **100**, 155–162.

Pedlosky, J., 1985: The instability of a continuous heton cloud. *J. Atmos. Sci.*, **42**, 1477–1486.

Raasch, S., and D. Etling, 1991: Numerical simulation of rotating turbulent thermal convection. *Contrib. Atmos. Phys.*, **3**, 1–15.

Rayleigh, O. M., 1916: On convection currents in a horizontal layer of fluid, when the higher temperature is on the lower side. *Philos. Mag. Ser. 6*, **32**, 529–546.

---

[10] Note that here the Prandtl number K_u/K_T has been set to unity from the outset.

Sankey, T., 1973: The formation of deep water in the northwestern Mediterranean. *Progress in Oceanography,* Vol. 6, Pergamon, 159–179.

Saunders, P. M., 1973: The instability of a baroclinic vortex. *J. Phys. Oceanogr.,* **3,** 61–65.

Schott, F., and K. D. Leaman, 1991: Observations with moored acoustic Doppler current profilers in the convection regime in the Gulf of Lions. *J. Phys. Oceanogr.,* **21,** 556–572.

Stern, M., J. Whitehead, and B.-L. Hua, 1982: The intrusions of a density current along the coast of a rotating fluid. *J. Fluid. Mech.,* **123,** 237–265.

Stommel, H., 1972: Deep winter-time convection in the Western Mediterranean Sea. *Studies in Physical Oceanography, A Tribute to Georg Wust on his 80th Birthday,* A. L. Gordon, Ed., Gordon and Breach, 207–218.

——, A. Voorhis, and D. Webb, 1971: Submarine clouds in the deep ocean. *Amer. Sci.,* **59,** 717–723.

Swallow, J. C., and G. F. Caston, 1973: The preconditioning phase of MEDOC 69. Part I: Observations. *Deep-Sea Res.,* **20,** 429–448.

Veronis, G., 1958: Cellular convection with finite-amplitude in a rotating fluid. *J. Fluid. Mech.,* **5,** 410–435.

Voorhis, A. D., and D. C. Webb, 1970: Large vertical currents observed in a winter sinking region of the northwestern Mediterranean. *Cah. Oceanogr.,* **22,** 571–580.